Slovak University of Technology in Bratislava
Faculty of Electrical Engineering and Information Technology

MSc. Niloofar Ebrahimzadeh Esfahani

Dissertation Thesis Abstract

Metal film coupled nanoparticle sensor platform based on plasmonic effect

to obtain the Academic Title of Philosophies doctor (PhD.)

in the doctorate degree study program: Electronics and Photonics
in the field of study: Electrotechnics
Form of Study: Full-time

Place and Date: Bratislava.21.2.2025

Dissertation Thesis has been prepared at the Institute of Electronics and Photonics, Faculty of Electrical Engineering and Information Technology, Slovak University of Technology in Bratislava.

Submitter: MSc. Niloofar Ebrahimzadeh Esfahani

Institute of Electronics and Photonics
Faculty of Electrical Engineering and Information Technology
Slovak University of Technology in Bratislava
Ilkovičova 3, 81219 Bratislava

Supervisor: doc. Ing. Jaroslav Kováč, PhD
Institute of Electronics and Photonics
Faculty of Electrical Engineering and Information Technology
Slovak University of Technology in Bratislava
Ilkovičova 3, 81219 Bratislava

Readers: prof. Dusan Pudis, PhD.
Department of Physics
University of Žilina
Univerzitná 1, 010 26 Žilina

prof. Alexander Kromka, DrSc
Insititue of physics
Czech academy of science
Narodni 3, 110 00 Prague 1, Czech Republic

Dissertation Thesis Defense will be held on 21.2.2025 at 10:00 a.m.
at Faculty of Electrical Engineering and Information Technology, Slovak University of Technology in Bratislava, Ilkovičova 3, 81219 Bratislava

……..
Prof. Ing. Vladimír Kutiš, PhD.
Dean of FEI of STU
Ilkovičova 3, 812 19 Bratislava

Contents

Introduction

In nanophotonics, scientists are primarily concerned with researching various methods and structures that are capable of enhancing and confining light in nanoscale geometries. To this end, plasmonic has attracted considerable attention due to its ability to manipulate and control light at the nanoscale, leading to improved performance in sensing, imaging, energy harvesting and other technological applications [1-4]. The unique properties of plasmonic structures offer researchers a versatile toolbox for addressing the challenges and opportunities presented in the field of nanophotonics

Generally, plasmonic structures consist of a metal and a dielectric part. This metal part can be a thin film or nanoparticles (NPs). A thin metal film having coherent collective oscillation of free electron gas in the interface of metal and dielectric can be coupled to an external incident electromagnetic wave at their resonance frequency. This coupling results in the induction of the surface plasmon resonances (SPR) [5]. SPRs, travel along the interface of metal and dielectric films. However, SPRs cannot be directly excited by an incident optical wave since the propagation constant of the oscillating charge wave is always greater than the propagation constant of the optical wave in the dielectric. Therefore, the momentum of the incident light must be enhanced. To this end, some methods are suggested, including prism, grating, waveguide, and optical fiber coupling. On the other hand, SPRs can be most excited by incident transverse magnetic (TM) polarized light [6].

In the case of using metal NPs instead of a metal film, the generated electromagnetic field is localized around the particle. For more than one nanoparticle, they will be coupled in the separation distance of the NPs, which leads to the strong enhancement and high confinement of the electromagnetic field in these small areas [7]. Contrary to the excitation of the localized SPRs (LSPRs), light does not need to be polarized since it occurs due to scattering. Moreover, LSPRs do not need any special coupling configuration to be excited. However, they still suffer from their small active volume corresponding to the field enhancement relative to the overall volume. It could limit their sensing application, especially for low-concentration samples. Moreover, there are some limitations in controlling the separation distance of the particles in the fabrication process [8].

Recently, a new configuration called film-coupled-nanoparticle has been introduced and studied in different areas [9-11]. This structure consists of a metal film, a thin dielectric gap film, and metal NPs. In this configuration, there are different possibilities, including the coupling of the metal NPs to their image on the metal mirror results in a strong field enhancement in the gap layer which is the main concern in this work [12], coupling between the localized and delocalized modes at the same time [13] and using induced propagating SPRs instead of the external incident light for excitation of the LSPRs which leads to a stronger field enhancement between the particles [14-16]. All these possibilities make utilizing this configuration a good choice in different areas. They can be used as surface-enhanced Raman spectroscopy (SERS) platforms [17]. Another application of such structures is utilizing them as plasmonic nano-rulers since they can probate nanoscale molecular dynamics due to their extreme sensitivity to the thickness of the gap layer between the metal film and NPs [13].

Such structures have been extensively studied due to their unique out-of-plane near-field coupling between the metal nanoparticles and the metal film (or the nanoparticles' images in the metal film). This strong coupling leads to the strong electric field enhancemnt within the gap layer and the coupling's strength can be easily tuned by adjusting the thickness of the dielectric spacer using readily available methods, such as atomic layer deposition (ALD). Significant efforts have been made to utilize these structures to enhance either optical absorption or the local electric field [18-23]. However, despite these advances, achieving both strong local field enhancement ($|E|/|E_0| > 100$) and near-perfect absorbance (>95%) remains a challenge, yet it is critical for many applications.

The intriguing properties and the aforementioned challenges of such structures motivated us to conduct a study on different configurations and explore various aspects of these structures. In this work, we examine nanostructures of various shapes and sizes to optimize all parameters for achieving the strongest electric field enhancement and near-perfect absorptance. Additionally, another goal of this study is to explore the sensing capabilities of such structures. To achieve this, some structural parameters are varied and optimized.

Goals of the thesis

1. **Optimize Plasmonic Nanostructures**: Design and analyze metal-insulator-metal (MIM) configurations to achieve strong electric field enhancement and near-perfect absorptance in visible and near IR optical spectrum.
2. **Investigate Coupling Mechanisms**: Study the interplay between surface plasmon polaritons (SPPs) and localized surface plasmon resonances (LSPRs), focusing on their dependence on geometry and material properties.
3. **Enhance Sensing Capabilities**: Explore the potential of plasmonic nanostructures for refractive index sensing, emphasizing their sensitivity to variations in the gap layer thickness and nanoparticle geometry.
4. **Develop Fabrication Techniques**: Employ methods such as thin film deposition, atomic layer deposition (ALD), and colloidal lithography to create precise and reproducible nanostructures.
5. **Validate Designs Experimentally**: Fabricate and characterize plasmonic structures, such as nanodisk and nanohole arrays, to confirm simulation predictions and assess their practical applications.

1 Simulation results

1.1 Gold nano-ellipsical particles over a metal film

In this work, the main purpose is coupling the NPs to their induced dipole image in the metal film as shown on Figure 1.1. In this regard, particles separation plays a crucial role on the resulted field enhancement in the dielectric layer between the NPs and metal film. While there is not too much attention to this important factor in related works and it has not been categorized as an effective parameter. More precisely, a larger separation distance compared to the size of the NPs can reduce the probability of the LSPR coupling between the particles. It solves the mentioned problem of controlling separation distance in the case of short distances. Therefore, to optimize the separation distance of the NPs, normal components of the electric field along various cutlines through the structure and for different particle separations have been studied by considering metal film and metal NPs made of gold. The proposed structure has potential application as plasmonic receiving nano antennas due to the strong absorption and enhancement of the incident light into an ultrathin dielectric layer. This characteristic feature also leads to a high-quality Raman spectrum, making this structure promising as a SERS platform. Moreover, due to the strong field enhancement in the dielectric layer, a change in the refractive index of the dielectric or geometrical parameters of the layer could lead to a change in the resonance frequency of the structure, which is promising for sensing applications.

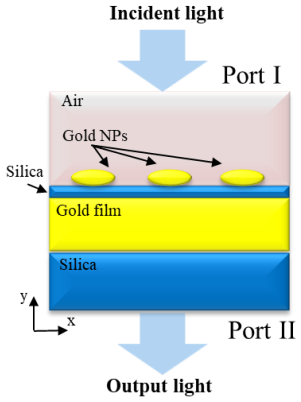

Figure 1.1 2D schematic of the proposed plasmonic structure

Design and simulation of the proposed structure are done by the wave optic module of COMSOL Multiphysics. As shown in Figure 1.1, the device consists of a gold layer and elliptical gold nanoparticles separated by an ultrathin SiO_2 dielectric layer with glass silica as the substrate of the whole structure. Permittivity (ε_s) of the silica defined as a function of the incident light wavelength (λ) can be calculated as follows:

$$\varepsilon_s = 1 + \frac{a_1\lambda^2}{\lambda^2 - b_1^2} + \frac{a_2\lambda^2}{\lambda^2 - b_2^2} + \frac{a_3\lambda^2}{\lambda^2 - b_3^2} \qquad 4.1$$

where $a_1 = 0.696749$, $a_2 = 0.408218$, $a_3 = 0.890815$, $b_1 = 0.0690660\ \mu m$, $b_2 = 0.115662\ \mu m$, $b_3 = 9.900559\ \mu m$ are material constants [24]. The Refractive index of gold is defined as a function of the wavelength based on the experimental data (Johnson and Christy 1972: n, k 0.188-1.937 μm) in the COMSOL material library.

A scattering boundary condition was imposed on all boundaries along the y-axis of the structure. In this way, all the boundaries along the y-axis are transparent for the incident light. In the COMSOL simulation, the wavelength of the incident light varies from

500 nm to 600 nm as a parametric sweep in the visible range area. The gold film's thickness is set at 30 nm, while the silica dielectric layer is just 2 nm thick. The longer diameter of the elliptical gold nanoparticles is set on 25 nm and their shorter diameter is 12 nm and their separation distance is 20 nm. Light enters the system at port one and exits at port two. Gold nanoparticles are surrounded by air that could be replaced with analyte material in sensing application. The refractive index of the air is set as $n_{air} = 1$.

Figure 1.2 indicates the distribution of the normalized electric field in the y direction in the proposed structure at resonance wavelength ($\lambda = 585$ nm). The thickness of the metal layer is 30 nm, the dielectric layer is 2 nm, and the separation distance of the particles is 20 nm. The main goal of this study is the coupling strength between the metal film and nanoparticles which is the reason for the adoption of declared separation between the particles. In other words, the separation distance must be large enough compared to the dielectric layer thickness to decrease the effect of the coupling between the LSPRs of the particles. Purpose coupling will be established in the dielectric layer, as obvious in Figure 1.2, in the shape of hot spots in that area. Two ellipses drawn with red dashed lines in the metal film represent the induced image of the particles. These induced images have opposite dipole with the real particles dipole as shown in inset pictures inside Figure 1.2.

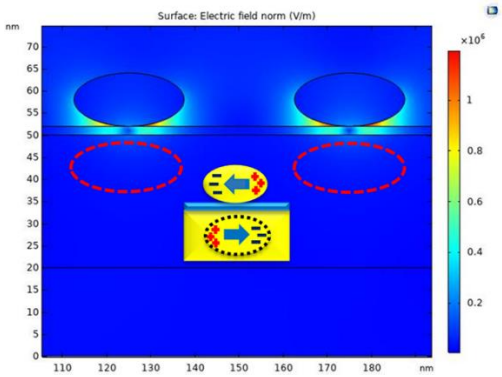

Figure 1.2 The normalized electric field

To study the influence of the metal film thickness on the resonance wavelength, the absorptance spectrum of the structure is derived in the graph in Figure 1.3 for thicknesses of 10 nm, 20 nm, and 30 nm. It demonstrates that decreasing the thickness from 30 nm to 20 nm leads to a decline in total absorptance, as expected. However, this thickness modification does not significantly affect the resonance wavelength of the structure. Decreasing the thickness from 20 nm to 10 nm, which is less than the dimension of the metal nanoparticles, leads to the resonance wavelength shift to longer wavelengths by 5 nm.

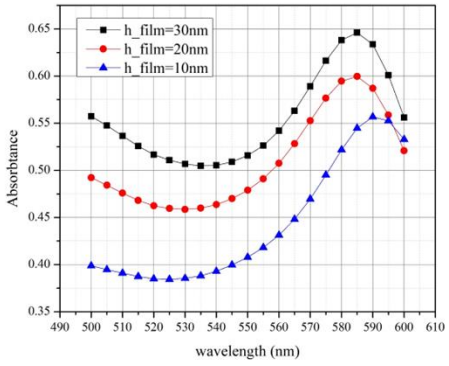

Figure 1.3 Absorptance spectrum of the structure for different metal film thicknesses of 10, 20, and 30 nm

As mentioned in all the previous written works in this field of research, the thickness of the dielectric layer plays an important role in the plasmonic properties of such structures. To observe this effect on the resonance wavelength of the LSPRs, the gap layer thickness was decreased from 10 nm to 2 nm for the proposed wavelength range shown in Figure 1.4. As obvious, by decreasing the thickness, the resonance wavelength is shifted to the longer wavelengths, and the FWHM of the absorptance peak is smaller, which is beneficial for sensing applications.

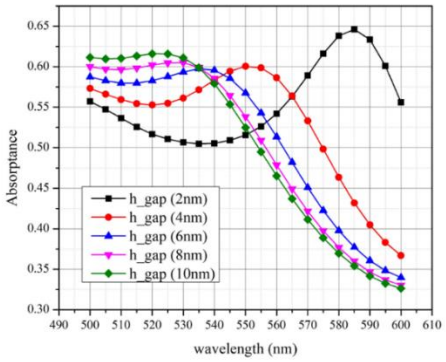

Figure 1.4 Absorptance spectrum of the structure with different gap layer thicknesses of 2,4,6,8 and 10 (nm)

To achieve strong LSPR and, consequently, strong field enhancement in the dielectric layer, nanoparticle separation should be large enough compared to the gap layer thickness. Figure 1.5 shows simulation results for particle separations varied from 5 nm to 30 nm, where a normalized electric field is studied. In each pair of graphs (for instance, a and b), different field distributions for the same particle separation but along different axes are demonstrated, as explored in inset pictures (along dashed yellow and red lines). As shown in Figure 1.5.a, when particle separation is as small as the dielectric layer thickness, LSPR coupling between the particles plays an important role. Another point in this picture is the induction of the SPR at the interface of the metal film and dielectric layer, which decays by increasing the distance from the interface, as expected. However, this SPR mode is insignificant compared to the LSPR mode between the particles. Comparing the graphs in Figure 1.5.a and 4.5.b shows the electric field in the dielectric layer due to the coupling of the LSPR mode II of the particle. Its dipole image in Figure 1.5.b is not as strong as the electric field between the particles shown in Figure 1.5.a. A closer look at the graph in Figure 1.5.b reveals that two LSPR modes are also obvious in the inset picture, as two hot spots at the bottom of the particle and in the gap layer are visible. The graphs indicate that the normalized electric field intensity related to the LSPR mode I is stronger than LSPR mode II. Maxwell's continuity conditions could explain the reason. Based on these continuity conditions, the normalized electric displacement ($\vec{D} = \varepsilon\vec{E}$) requires to continue across the interface between two materials. Consequently, the normalized electric field in the air will be larger than its value in the dielectric layer by a factor approximating the dielectric constant of the dielectric layer material. This can describe the reason for the compression in size of the hot spot in the dielectric layer as compared to the region between the dielectric layer and nanoparticles. However, even the maximum electric field intensity related to the LSPR mode I in Figure 1.5.b is still very close to the maximum electric field in the separation distance of the particles in Figure 1.5.a. To enhance the electric field in the gap layer, the separation distance is increased from 5 to 10, 15, 20, 25, and 30 nm, and the results are shown in Figure 1.5.c to 1.5.l. Increasing the separation distance decreases the electric field between the particles related to the LSPR coupling of the particles.

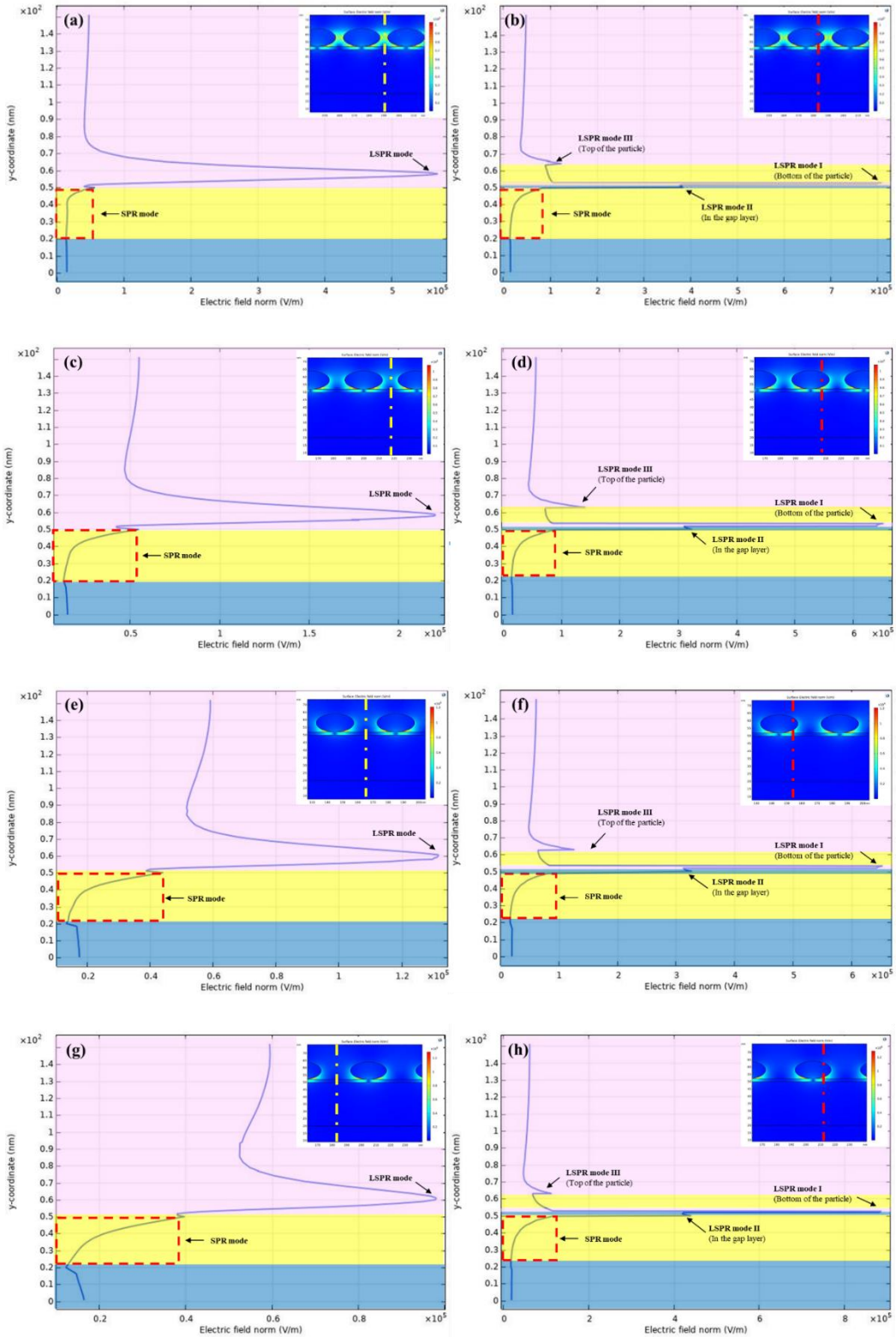
(a)
(b)
(c)
(d)
(e)
(f)
(g)
(h)
y-coordinate (nm)
Electric field norm (V/m)
LSPR mode
SPR mode
LSPR mode III
(Top of the particle)
LSPR mode I
(Bottom of the particle)
LSPR mode II
(In the gap layer)

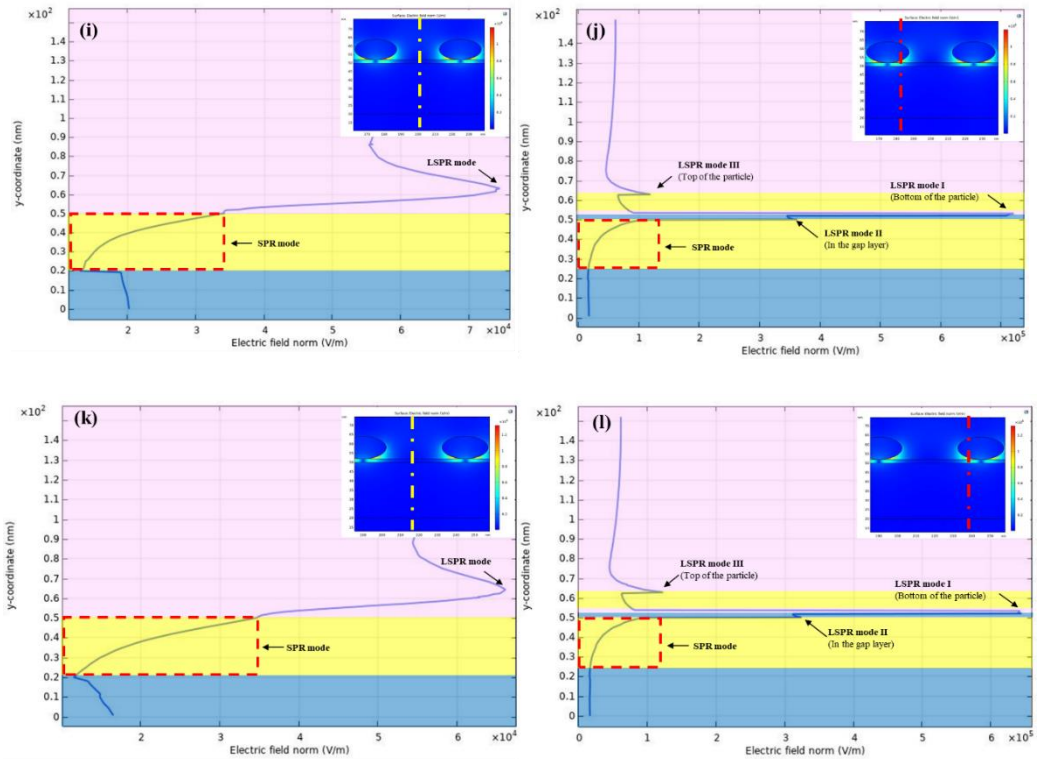

Figure 1.5 . Normalized electric field along two different cutlines for different particle separations of 5 nm (a,b), 10 nm (c,d), 15 nm (e,f), 20 nm (g,h),25 nm (I,j) and 30 nm (k,l).

On the other hand, the electric field in the dielectric layer and from its interface to the bottom of the particle (along the yellow dash line passing through the particle) is increased in both cases until the separation distance of 20 nm. It begins to decline after increasing the separation from 20 nm to 30 nm by a factor of $2*10^5$ V/m. This declining trend after 20 nm might be due to the possibility of considering nanoparticles as single particles when they have a very large separation distance (more than 20 nm). Accordingly, the influence of more than one nanoparticle in field enhancement is larger than that of a single nanoparticle. By increasing the separation distance of the particles, the normalized electric field related to the SPR mode at the metal-dielectric interface along the axis passing through the separation distance of the particles is decreased from $9*10^4$ V/m to $6*10^4$ V/m. This decreasing trend might be because, in the case of smaller separation, the particles can be considered as an array that fulfils the coupling condition needed for the excitation of the SPRs. By increasing the separation of the particles, each particle can be considered as a single particle, and the probability of the SPR induction is decreased. However, this increasing separation does not significantly affect the normalized electric field's related to the SPR mode, along the axes passing through the particles and it remains around 10^5 V/m. The reason might be related to the important role of the LSPRs in the dielectric layer.

LSPR mode III in Figure 1.5.b, d, f, h, j, l represents the LSPR mode on the top of the particles, which is not coupled and declined by increasing separation of the particles.

1.2 3D structure with gold nanodisks and nanostrip arrays over a gold film

Metallic nanoparticles tend to aggregate, impacting their plasmonic properties and stability over time. To manage this, replacing nanoparticles with periodic metallic nanoarrays is crucial. These periodic nanostructures offer precise control over plasmonic resonances by adjusting their dimensions, thus meeting specific sensor application needs[25]. Various periodic metal nanostructures have been reported, featuring different shapes and sizes, such as nanodisks with triangular, circular, and square intersections, as well as periodic metal nanostrips with rectangular intersections. While these nanodisks and nanostrips may appear similar in two-dimensional simulations, exhibiting identical intersections, three-dimensional simulations reveal significant differences. Therefore, studying and comparing these structures to uncover their similarities and differences is crucial for designing plasmonic structures, particularly metal-insulator-metal (MIM) nanoantennas with periodic metallic arrays. Understanding these distinctions can lead to optimized designs with enhanced performance. Metal nanostrips provide a high signal-to-noise ratio and accurate measurements due to their larger size and strong plasmonic resonances. They allow precise control over hotspots and the electric field, enhancing targeted applications. Their anisotropic nature offers design flexibility for directional responses [26-28]. Metallic nanodisk arrays, with their circular shape, exhibit unique plasmonic behavior. They are particularly useful in surface-enhanced spectroscopy, sensing, and imaging due to their strong local field enhancement. as mentioned above, despite similar 2-dimensional intersections, the 3-dimensional shapes of nanodisks and nanostrips differ, necessitating a comparative study to explore their similarities and differences for effective plasmonic structure design, especially in MIM nanoantennas.

Significant efforts have been devoted to using metal-insulator-metal (MIM) structures to enhance optical absorption and local electric field. MIM nanoantennas, which exhibit simultaneous electric and magnetic responses to incident light, are extensively used as perfect metamaterial absorbers (PMAs) in the near-infrared (NIR) and visible regions[18, 19]. For example, Chu et al. developed an MIM-structured surface enhanced Raman scattering (SERS) substrate with a circular nanodisk array, achieving a maximum electric field enhancement of nearly 86 [20]. Similarly, Seok et al. demonstrated an electric field enhancement of 87 in an MIM optical antenna with a nanorod dimer array[21]. However, low area fill factors reduce the density of "hot spots" and decay light absorbance due to the dilution effect, typically resulting in less than 60% absorbance. Recent developments have focused on MIM PNs with sub-3 nm thick spacers to achieve strong field localizations. Lassiter et al. achieved a 90% absorbance and a calculated field enhancement of 57 using film-coupled gratings with a 2.83 nm thick spacer [29]. Huang et al. compared MIM plasmonic cavities with various nanoparticle shapes and attained a field enhancement above 100 in a nanorod cavity with a 2 nm spacer [30]. Despite these advances, achieving both strong local field enhancement ($|E|/|E_0| > 100$) and near-perfect absorbance (>95%) remains challenging but crucial for many applications.

This study explores the design and simulation of two MIM plasmonic nanoantennas—periodic circular nanodisks and rectangular nanostrip arrays—using the Wave Optics module of COMSOL Multiphysics. By optimizing geometrical parameters and analyzing polarization effects, the structures demonstrated enhanced plasmon coupling, light absorption, and electric field enhancement. Both structures exhibited multiple plasmonic resonance modes, with nanodisks excelling at dipole resonance and nanostrips offering sharper higher-order modes for precise sensing. FEM-based simulations integrated Maxwell's equations and material models to evaluate optical responses and sensing capabilities, highlighting the potential of these structures for advanced sensing and field enhancement applications.

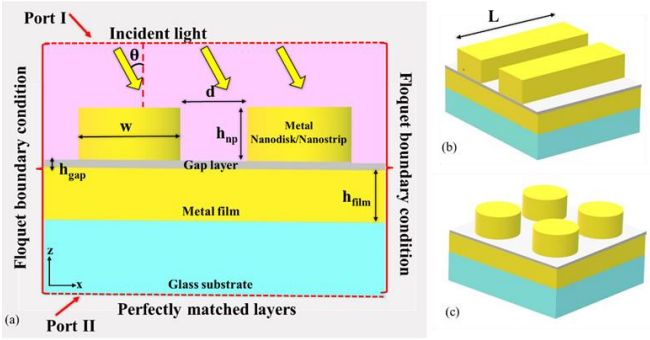

Figure 1.6 (a-c) Schematics of the plasmonic structures: (a) 2D layout of periodic metal nano-disk/nano-strip array, (b) 3D view of the nanostrip array, and (c) 3D view of the nanodisk array. h_{film} = metal film thickness, h_{np}= the height of the nano-disk/nano-strip , h_{gap}=gap layer thickness, d = separation distance between the nano-disks/nano-strips ,w= diameter/width of the nano-disk/nano-strips and L is the length of the nanostrips

Gold is selected as the plasmonic material owing to its distinct characteristics. It stands as the second least lossy metal within the visible spectrum after silver. Its superior chemical stability compared to silver makes it more desirable for plasmonic applications. The dielectric constant, or permittivity, of gold plays a crucial role in determining the behavior of localized surface plasmons (LSPs). Gold exhibits a notably large negative real part of permittivity in the visible and near-infrared ranges. This negative permittivity gives rise to significant resonances at specific wavelengths, resulting in enhancement electromagnetic fields surrounding the nanoparticles [31]. Regarding to the dielectric material, Al_2O_3 possesses a comparatively high dielectric constant, promoting robust confinement of electromagnetic fields within the insulator layer. This characteristic amplifies the interaction among the metal film and nanoparticles, thereby enhancement of the plasmonic effects. The deposition of aluminum oxide can be accomplished through diverse methods like atomic layer deposition (ALD) or sputtering, providing flexibility in fabrication techniques. This deposition ease enables precise control over the dielectric layer's thickness and uniformity, simplifying the fabrication of the plasmonic structure [32].

The metal film, 60 nm thick, is deposited on the substrate using methods like physical vapor deposition, while the 5 nm Al_2O_3 layer is applied via atomic layer deposition (ALD). For Al_2O_3 layers thinner than 5 nm, quantum effects significantly alter the plasmonic response due to nonlocal screening, as noted by Wenqi Zhu et al. [33]. In the simulations, the height of nanostrips and nanodisks and the thickness of the metal film were optimized for maximum absorptance. The nanodisks and nanostrips have fixed dimensions of 80 nm, with 30 nm spacing to minimize localized surface plasmon coupling, and nanostrip depth is assumed infinite due to periodic Floquet boundary conditions.

To gather the complete near-field spectral characteristics and identify the resonance wavelength where maximum near-field enhancement occurs, we utilize average near-field enhancement spectroscopy in this paper. This spectroscopy is achieved by averaging the volume integral of $|\mathbf{E}|^4/|\mathbf{E}_0|^4$ [34, 35]:

$$EF = \frac{\iiint \frac{E^4}{E_0^4} . dV}{V} \qquad 4.2$$

Where V is the volume of the gap layer, E is the scattered electric field and E_0 is the incident electric field. It is established that the enhancement factor (EF) of Surface Enhanced Raman Scattering (SERS) is roughly proportional to the fourth power of the local electric field intensity $|\mathbf{E}|^4/|\mathbf{E}_0|^4$. Consequently, the EF can be interpreted as the averaged electromagnetic enhancement factor

of SERS, assuming that the adsorbed Raman probe molecules are distributed randomly and uniformly on the surface of metal nanoparticles. To compare the sensing capability of the structures, their refractive index sensitivity (S) which is defined as:

$$S = \frac{\Delta\lambda}{\Delta n} \qquad 4.3$$

expressed in nanometers per refractive index unit (nm/RIU), where ($\Delta\lambda$) is the shift of the resonant peak wavelength of absorption and (Δn) is the refractive index difference of the analyte material[1].

1.2.1 Structure optimization

Optical absorptance is the fraction of incident light that is absorbed by a material or structure instead of being reflected or transmitted. In the context of plasmonic structures, absorptance is a key parameter that quantifies the efficiency with which these structures convert incident light into localized surface plasmons, resulting in enhanced electromagnetic fields and energy dissipation within the material. Figure 1.7 provides a detailed examination of the absorptance characteristics of plasmonic structures comprising metal nanostrip and nanodisk arrays, and illustrates how the height of the nanoparticles affects absorption at different wavelengths. The 2D plot in Figure 1.7(a) shows the absorptance as a function of nanoparticle height (h_{np}) and wavelength for the nanostrip array structure. As shown, there is a pronounced absorptance peak at about 500 nm for a nanoparticle height of 50 nm and a narrow peak around 1100 nm for a nanoparticle height of 30 nm. In addition, a moderate increase in absorptance can be observed at 630 nm for a nanoparticle height of 70 nm, shown in orange. The 3D visualization in Figure 1.7(b) shows more clearly how the absorptance varies with nanoparticle height and wavelength, highlighting the sharpness and intensity of the absorptance peaks.

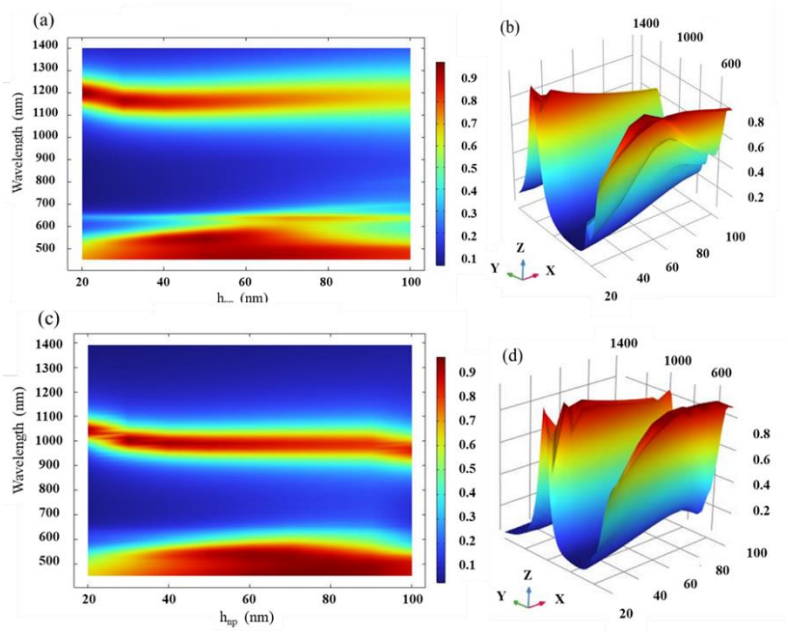

Figure 1.7 (a) 2D plot showing the absorption as a function of nanoparticle thickness and wavelength for the nanostrip array structure. (b) 3D visualization of absorptance variation with nanoparticle thickness and wavelength for nanostrip arrays, emphasizing sharpness and intensity of absorption peaks, (c) 2D plot of absorption as a function of nanoparticle thickness and wavelength for nanodisk arrays. (d) 3D visualization of absorptance variation with nanoparticle thickness and wavelength for nanodisk arrays, highlighting the distribution of absorption peaks.

The plot in Figure 1.7(c) follows the format of part (a), but for nanodisk arrays. In this structure, a strong peak around 500 nm is observed for a nanoparticle height of 80 nm and a significant peak around 1000 nm for a height of 30 nm. The 3D representation in part (d) improves the visualization of the distribution of these absorptance peaks over the height of the nanoparticles and wavelength. The difference in the optimal height for the 500 nm peak between nanostrips and nanodisks indicates that the circular geometry of the nanodisks affects the plasmonic resonance differently, probably due to variations in field confinement and surface plasmon distribution. The comparison between Figure 1.7(a,b) and 4.7(c,d) underlines the influence of the geometry of nanostructures on the plasmonic behavior. Due to their different shapes, nanostrips and nanodisks support different plasmonic modes that respond to the height of the nanoparticles, as shown by the shift in the optimal height for peak absorptance in each configuration. The ability to tune absorptance peaks by adjusting the height of nanoparticles provides a versatile tool for optimizing nanoantenna designs. This tunability is particularly valuable for applications that require precise control over the wavelength of peak absorptance, as different applications may require different spectral responses.

Figure 1.8 provides a revealing illustration of how the absorptance properties in plasmonic structures with metal nanostrip and nanodisk arrays are influenced by changes in metal film thickness at different wavelengths. The 2D plot in Figure 1.8(a) shows the absorptance as a function of metal film thickness (h_{film}) in the range from 20 nm to 100 nm and wavelength. A clear increase in absorptance can be observed for metal films with a thickness of up to 60 nm, which is particularly noticeable at wavelengths of 1100 nm and 500 nm. For example, the absorptance at 500 nm rises sharply to around 0.85 at a film thickness of 50 nm. Beyond 60 nm, the rate of increase in absorptance decreases significantly and stabilizes around an absorptance value of 0.9, which indicates a saturation effect in the plasmonic enhancement. The maximum absorbance at 1100 nm consistently exceeds that at 500 nm, indicating a stronger plasmonic resonance at the longer wavelength. At 630 nm, there is an increase in absorptance (peak value around 0.4), which remains relatively unchanged with a further increase in metal layer thickness. The 3D plot in part (b) provides a spatial representation of these trends and visually highlights the thickness regions where the changes in absorptance are most pronounced, as well as the saturation beyond 60 nm.

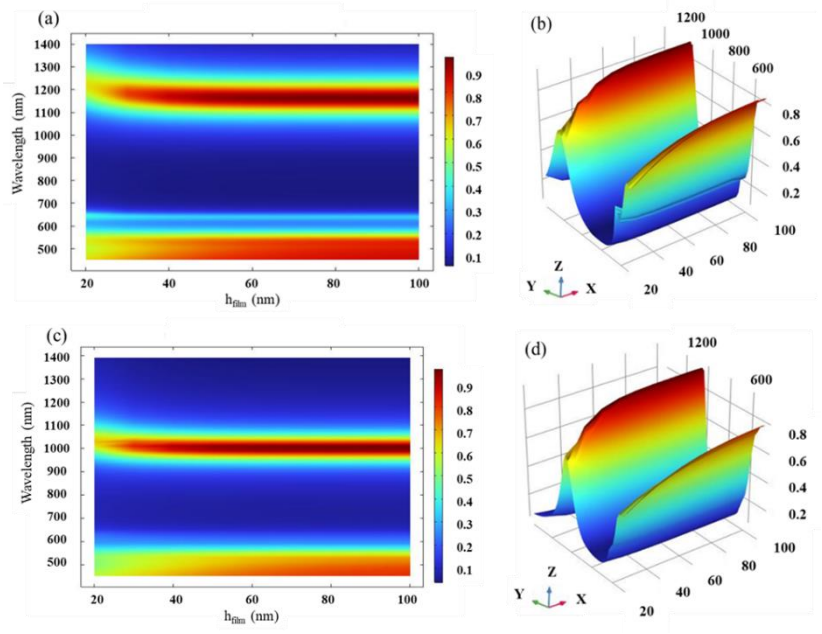

Figure 1.8 (a, c) 2D plots depicting absorptance as a function of metal film thickness for (a)nanostrip and (c)nanodisk arrays, with notable absorptance increases up to 60 nm thickness, (b, d) 3D visualizations of absorptance variation with metal film thickness for (b) nanostrip, and (d) nanodisk arrays, indicating absorptance stabilization beyond 60 nm.

Similar to part (a), the plot in part (c) shows the absorptance at different metal film thicknesses for nanodisk arrays. In this structure, the absorptance is increased at a metal layer thickness of 20 nm to 60 nm, and significantly at wavelengths of 1000 nm and 500 nm. For example, the absorptance at 1000 nm increases to about 0.88 at a thickness of 50 nm. Beyond 60 nm, similar to the nanostrips, the trend hardly changes, indicating saturation. As with the nanostrips, the absorptance maximum at around 1100 nm exceeds that at 500 nm. The 3D visualization in part d highlights the variations of the absorptance with the thickness of the metal film and the wavelength and emphasizes the stability of the absorptance after 60 nm thickness. Figure 1.7 and 4.8 emphasize the importance of structural dimensions (nanoparticle and metal film thickness) in modulating plasmonic responses. The observed saturation of absorptance beyond 60 nm for different configurations indicates a threshold for effective plasmonic enhancement.

Figure 1.9 shows the 2D plot of the absorptance spectrum for both proposed structures as a function of the angle of incidence (θ, measured from the perpendicular to the xy plane) at transverse magnetic (TM) polarization. In Figure 1.9(a), the fundamental resonance wavelength of the structure with a nanostrip array shows no significant shift as the incident angle increases from 0 to 40 degrees. However, it is obvious that within this range, the maximum absorptance decreases, with the strongest absorptance occurring at zero degrees. As the angle of incidence increases from 40 to 80 degrees, a clear shift towards shorter wavelengths is observed in the resonant mode of the structure, accompanied by weaker absorptance.

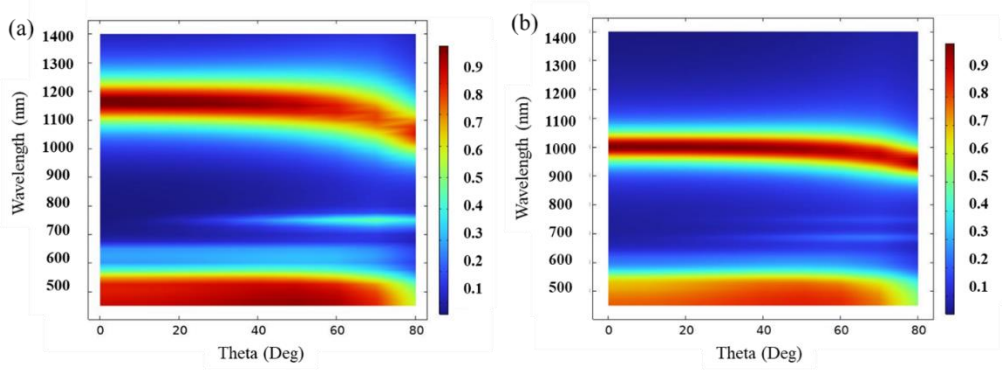

Figure 1.9 2D plots depicting absorptance as a function of incident light angle for (a) nanostrip and (b) nanodisk arrays under TM polarization.

As for the structure with the nanodisk array, Figure 1.9(b) shows a similar trend to the nanostrip array, but with some differences in absorptance and resonance wavelength shift. In this case, the shift occurs at a longer wavelength for more than 60 degrees of light incidence. Another important point when comparing this structure with the nanostrip array is that the nanodisk array has a smaller shift in resonance wavelength and a less significant decrease in absorptance as the angle of incidence increases. Nevertheless, for both structures, the maximum absorptance is reached at an angle of incidence of zero degrees. At this angle, the nanodisk array achieves an absorptance of about 0.95 for its fundamental plasmonic mode, compared to about 0.90 for the nanostrip array. The enhanced performance of the nanodisk array can be attributed to its symmetric shape, which may provide more uniform interaction with incident light at varying angles, compared to the more directional nanostrip array. This behavior is critical for applications requiring high angular tolerance, such as in solar energy harvesting or sensing devices. These observations highlight the superior angular performance of nanodisks and emphasize the importance of considering angular sensitivity in the design of plasmonic nanoantennas. Integrating these findings with previous insights on structural parameters, such as nanoparticle height and metal film thickness, offers a comprehensive understanding of how geometry influences light interaction across different wavelengths and incident angles.

The optimization of the height of the nanoparticles, the thickness of the metal film and the angle of the incident light shows that despite the different shapes of the nanoparticles, both structures show their best performance with the same optimized parameters. This similarity could be due to their identical cross-sectional view in the xz-plane, as shown in Figure. 4.6(a). This indicates that a two-dimensional simulation can be effectively used to optimize these parameters. However, when comparing the overall performance, the differences between the two structures become apparent and a three-dimensional simulation is required for a comprehensive evaluation. This dual approach ensures both efficiency in optimization and thoroughness in performance evaluation, paving the way for the practical use of these plasmonic structures in various technological applications.

1.2.2 Electric field enhancement

The enhancement of the electric field in plasmonic structures is of crucial importance due to its diverse applications and effects. This enhancement is particularly important in the near-field region, close to the surface of the plasmonic structures. Comparing the electric field enhancement in different plasmonic structures allows researchers and engineers to understand the underlying physics and identify optimal designs for specific applications. Figure 1.10(a) shows a comprehensive investigation of the electric field enhancement factors calculated with Eq. 4.2 for both structures under different polarizations (TM and TE). To visualize the electric field distribution in the gap layer at the plasmonic fundamental mode for different polarizations and to compare the electric field enhancement, the distributions of the ratio of the scattered electric field to the incident electric field for plasmonic nanostructures with nanostrip and nanodisk arrays are simulated and shown in Figure 1.10(b-e). It is important to note that the optimized structure parameters, including h_{np} = 30 nm, h_{film} = 60 nm, and an incident angle of zero degrees, were used for the simulation results shown in the following sections.

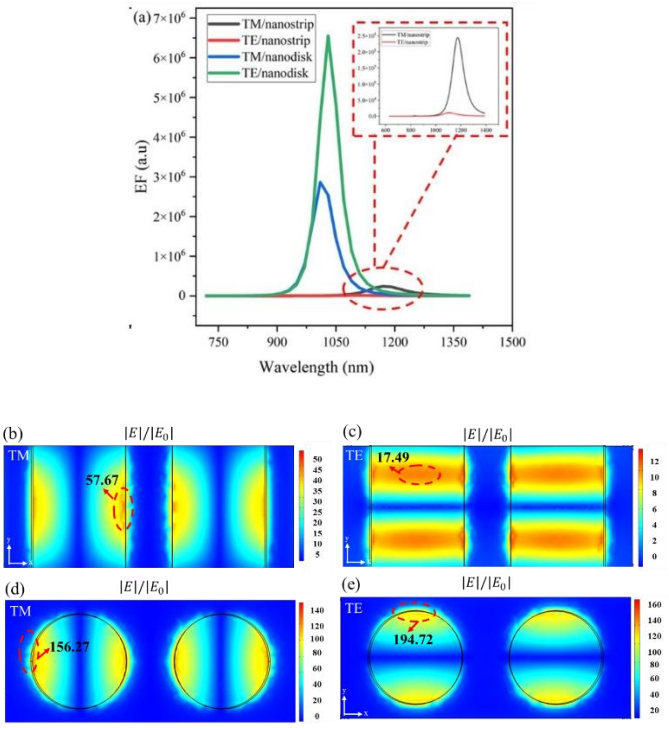

Figure 1.10 (a)Electric field enhancement factors for nanostrip and nanodisk arrays under TM and TE polarizations. Top view visualization of the electric field distribution in the gap layer for nanostrip arrays under (b) TM polarization and (c) TE polarization. Top view visualization of the electric field distribution for nanodisk arrays under (d) TM polarization and (e) TE polarization.

Figure 1.10(a) shows clear peaks in the field enhancement factors as a function of polarization and structure type. TE polarization with nanostrip arrays exhibits a much lower enhancement factor of 1.5×10^4 at 1080 nm, indicating poor interaction with the electric field at this polarization. In contrast, TM polarization is more effective with this structure, showing an electric field enhancement of about 2.5×10^5 at 1160 nm. The inset plot provides a focused view of the field enhancement factor for the nanostrip array under different polarizations at their dipolar resonance wavelength, highlighting the strong contrast between TM and TE modes. For nanodisk arrays, the TM polarization shows a significant peak around 1000 nm with a field enhancement factor of 2.8×10^6, while the TE polarization for the same structure shows an even higher field enhancement factor of 6.6×10^6 at 1030 nm, which is significantly larger than its TM counterpart. The observed differences in field enhancement between nanostrips and nanodisks at different polarizations are due to their different geometries and how these geometries interact with the incident electric field. The elongated shape of the nanostrips fits better with TM polarization, while the symmetric nanodisks show better performance at TE polarization due to more effective coupling and confinement of the electric field.

Figure 1.10(b) shows a strong field localization along the length of the nanostrips in TM polarization, with a maximum ratio of 57.67. In contrast, TE polarization shows a weaker and more distributed field enhancement with a maximum ratio of 17.49, which is consistent with the lower enhancement factors observed in part (a). In part (d), TM polarization for nanodisk arrays shows robust field confinement around the perimeter of the disks, although not as strong as for TE polarization. The TE polarization for nanodisk arrays in part (e) shows extremely strong field localization at the edges of the nanodisks, which is consistent with the observed high enhancement factor. The maximum ratio for TM polarizations in the nanodisk structure is 156.27, and it is 194.725 for TE polarization which is significantly higher compared to the values reported in previous studies [9, 20, 30] for circular nanodisks and other shapes such as cubes, spheres, and rods. This result shows how the optimization of nanodisks and metal layer thickness affects the electric field enhancement.

1.2.3 Sensing properties

To complete the comparison of the two structures, their sensing ability was evaluated after examining their field enhancement and near-perfect absorptance properties. In this evaluation, the refractive index (RI) of the analyte located around the nanoparticles (instead of air) varied from 1.33 to 1.63 and the absorptance spectrum of the structures was simulated. It is important to clarify that the actual RI detection range of the proposed structure is determined by the resonance wavelength shifts and the sensitivity of the structure. While the simulations in this study focused on the range of 1.33 to 1.63, the structure has the potential to detect RI values slightly beyond this range, depending on the specific application and sensitivity required. However, sensitivity and accuracy may decrease outside of the tested range, which is why this specific interval was emphasized in this work.

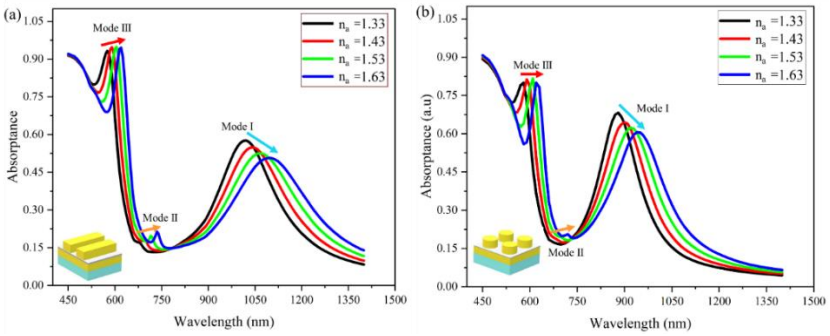

Figure 1.11 Simulated absorptance spectra for (a) nanostrip and (b) nanodisk arrays with varying refractive index of the dielectric layer from 1.33 to 1.63.

Table 1-1 Comparison of the sensitivity of the structures with nanostrip and nanodisk arrays in this study.

	S (nm/RIU) Mode I	S (nm/RIU) Mode II	S (nm/RIU) Mode III
Nanostrip	300	240	150
Nanodisk	300	-	100

Initially, no significant sensor characteristics were observed at a dielectric thickness of 5 nm. However, increasing the thickness to 10 nm led to noticeable changes in the resonance peaks for different analyte materials, as shown in Figure 1.11 for both structures. The resonance peaks in plasmonic structures can shift either to longer wavelengths (red shift) or to shorter wavelengths (blue shift), depending on specific changes in the structure or in the environment. A red shift typically occurs when the coupling between the plasmonic components increases, e.g. when the distance between the metal layers decreases, resulting in a stronger electric field and a longer resonance wavelength. Conversely, a blue shift can occur when the effective refractive index of the surrounding medium decreases or when the dimensions of the nanostructures are reduced, resulting in a shorter resonance wavelength. Both types of shifts are crucial for tuning the optical properties of plasmonic structures for different applications.

Figure 1.11(a) shows that the nanostrip array structure exhibits three distinct peak shifts in the resonant wavelength, indicating its suitability for sensing applications. In contrast, although the nanodisk array structure also shows three peaks, the second peak (Mode II) is not sharp and only becomes visible at a refractive index of 1.63, making it less suitable for sensing applications compared to the nanostrip array. To obtain detailed information about the sensitivity of the individual structures in the different modes, their sensitivity was calculated using Equation 4.3. The results are shown in Table 1.1. According to the data, the sensitivity of the two structures is similar in Modes I and III. However, in Mode II, only the nanostrip array structure shows its sensing capability. The sensitivity of these structures could be further improved by optimizing other parameters, such as the spacing and diameter of the nanoparticles or by increasing the dielectric layer thickness beyond 10 nm. The choice of a layer thickness of 10 nm for these structures is of strategic importance: it is thin enough to ensure strong field enhancement in the gap layer and at the same time thick enough to enable sensing capability. This balance is crucial to achieve both high field enhancement and effective sensing performance.

1.3 3D structure with gold nanohole structure over a metal film

Metallic nanohole arrays have gained significant attention due to their extraordinary optical transmission, which arises from the excitation of surface plasmon polaritons (SPPs) and localized surface plasmon resonances (LSPRs). These unique optical properties enable simultaneous excitation of propagating SPPs along the metal-dielectric interface and LSPRs confined to the edges of the nanoholes or other geometric features. This dual-mode excitation offers a sophisticated mechanism for manipulating light at the nanoscale, particularly in sensing applications [36-38].

In nanohole-dielectric-metal film structures, the interaction between the nanohole array and the underlying metal film through a dielectric gap layer results in hybridized plasmonic modes, including gap surface plasmon (GSP) modes. GSPs arise from the electromagnetic confinement within the gap, leading to enhanced electric fields and additional resonances. The hybridization of LSPRs, SPPs, and GSPs creates a rich spectrum of modes, each influenced by structural parameters. For instance, increasing the

dielectric gap thickness weakens the nanohole-film coupling, causing redshifts and broadening of hybrid modes. Similarly, changes in periodicity affect diffraction orders, altering resonance positions [37, 39, 40].

Compared to simpler nanodisk arrays, nanohole arrays provide enhanced transmission, higher refractive index sensitivity, and tunable plasmonic responses. This makes them advantageous for sensing and optoelectronic applications. Fabrication via lithographic techniques, such as nanosphere lithography, offers precise control over structural parameters. Furthermore, the combination of nanohole arrays with thin films broadens the variety of optical properties, particularly in MIM-type metasurfaces.

Through simulation and experimental comparison, the proposed nanohole-dielectric-metal film structure demonstrates its potential for high-performance plasmonic sensing. By leveraging the interplay of LSPRs, GSPs, and SPPs, these systems achieve exceptional field enhancement and environmental sensitivity, providing a robust platform for nanoscale optical manipulation and sensing [41]. Near-perfect absorption has been achieved across visible and near-infrared frequencies. The optical behavior of perforated MIM structures is often attributed to Fabry-Perot resonances and the resonant excitation. Due to their relatively simple structure, perforated MIM-type metasurfaces can be fabricated via lithographic methods, providing precise structural control down to the nanometer scale. Efforts are ongoing to develop solution-processed techniques for large-scale production, using self-assembly methods. Nanohole arrays coupled with thin metal films have been prepared using nanosphere lithography (NSL), with the primary resonance wavelength determined by both the nanohole array's grating equation and the Fabry-Perot condition. Additionally, structures like nanohole-dielectric-metal film configurations exhibit gap modes, broadening the scope of their optical properties[42]. Comparison of the plasmonic nanohole array and nanodisk array which is proposed in the last part shows plasmonic nanohole arrays provide enhanced transmission, higher refractive index sensitivity, and versatile tunability, making them advantageous for sensing, filtering, and optoelectronic applications. Nanodisk arrays, on the other hand, are simpler in design and fabrication but may not match the level of performance in applications requiring high transmission and sensitivity [42]. After evaluating various structures, considering all possibilities including accessible technology and equipment, and comparing simulation results, we propose, design, and simulate a nanohole-dielectric-metal film structure and evaluate its optical properties and sensing capability. In the next chapter, this proposed structure is fabricated in the laboratory, and the experimental results are presented and discussed. Through simulation and experimental comparison, the proposed nanohole-dielectric-metal film structure demonstrates its potential for high-performance plasmonic sensing. By leveraging the interplay of LSPRs, GSPs, and SPPs, these systems achieve exceptional field enhancement and environmental sensitivity, providing a robust platform for nanoscale optical manipulation and sensing.

The Finite Element Method (FEM) was used to simulate the absorption spectrum and normalized electric-field magnitude (Enorm) distribution of the proposed structure under varying parameters. TM-polarized detection light (400–1200 nm) was incident at the center of a single nanohole. The computational domain consisted of a glass substrate, an 80 nm gold thin film, a variable-thickness Al_2O_3 dielectric gap layer (5–40 nm), and a 40 nm gold layer with nanohole arrays, optimized through 2D simulations, with the top domain representing the external environment. Material optical properties were modeled using frequency-dependent dielectric functions, with gold's properties interpolated from Johnson and Christy’s experimental data. Surface plasmon activation was simulated using wavelength modulation with a linearly polarized electromagnetic wave. Boundary conditions at the simulation domain's edges enabled calculation of reflection and transmission coefficients.

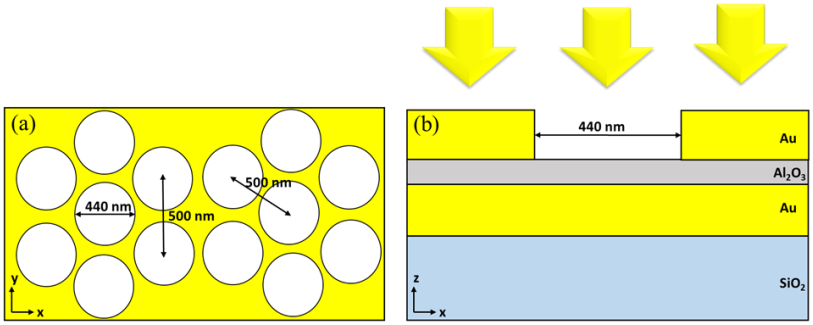

Figure 1.12. 2D illustration for the simulation model in (a) x-y plane and unit cell design in (b) x-z plane.

1.3.1 Structure optimization

Figure 1.13 presents a two-dimensional graph illustrating the absorptance spectrum of the plasmonic structure as a function of the radius of the nanoholes. In this analysis, the radius of the nanoholes is varied from 175 nm to 225 nm, a range selected to align with the experimental constraints of the study. This parameter range allows a practical comparison between the simulated and experimental results. The absorptance spectrum reveals two distinct peaks for each nanohole radius indicating as mode I and mode II. Among these, mode II consistently exhibits a stronger absorptance, while mode I remains weaker across the range. The purpose of generating this graph was twofold: first, to identify the optimal nanohole radius that maximizes absorptance, and second, to investigate how the resonant modes shift with changes in the nanohole radius, thereby providing insights into the origins of the plasmonic modes observed in the structure.

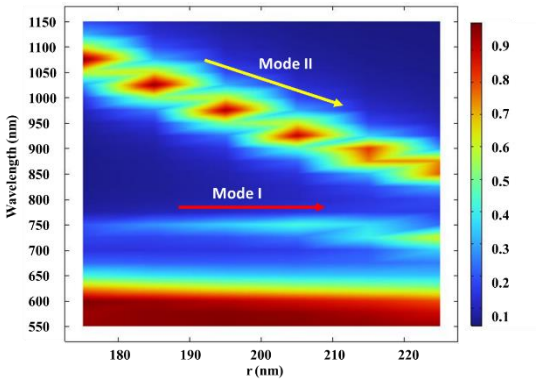

Figure 1.13 2D plot depicting the absorptance spectrum of the light as a function of the radius of the nanoholes

The results indicate that mode II exhibits a noticeable blue shift (toward shorter wavelengths) as the nanohole radius increases. In contrast, the weaker mode I remains largely stationary, showing no significant spectral shift. This behavior suggests that the mode II is either completely or partially associated with a localized surface plasmon resonance (LSPR) mode, as LSPRs are known to be highly sensitive to variations in the geometric parameters of the nanostructure. On the other hand, the lack of a shift in the mode I, strongly implies that it is not related to LSPR phenomena and likely arises from a different plasmonic mechanism.

It is worth noting that throughout this analysis, the thickness of the dielectric gap layer was held constant at 40 nm to isolate the effect of the nanohole radius on the plasmonic modes. The constant gap layer ensures that any observed shifts in resonance are attributable solely to changes in the radius, avoiding potential confounding effects from other structural parameters. To further

analyze the nature of these plasmonic modes and their dependence on different structural parameters, additional analyses were performed, as illustrated in the subsequent figures. By altering other variables, such as the thickness of the dielectric gap and tuning of the angle of incident light, a more comprehensive understanding of the modal behavior is achieved.

Figure 1.14 presents a two-dimensional plot illustrating the absorptance spectrum of the plasmonic structure as a function of the thickness of the dielectric gap layer. In this analysis, the gap layer thickness is varied from 10 nm to 60 nm with the holes diameter of 440 nm to investigate its impact on both the resonance wavelength and the strength of the absorptance peaks.

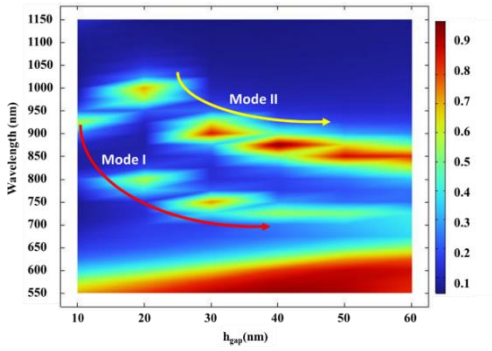

Figure 1.14 2D plot depicting the absorptance spectrum of the structure as a function of gap layer thickness (t_{gap})

The results clearly demonstrate that the gap layer thickness significantly influences the plasmonic behavior of the structure. As the thickness is increased from 10 nm to 40 nm, the resonance mode II exhibits a blueshift (shift to shorter wavelengths). While the resonance mode I persists, its absorptance diminishes slightly compared to thinner gap layers. At a thickness of 40 nm, the primary resonance achieves a balance between a relatively strong absorptance and a stable resonance wavelength. Beyond this point, as the gap layer thickness is increased to 60 nm, a decrease in absorptance is observed for both resonance modes. The resonance mode II continues to blueshift, while the resonance mode I becomes increasingly weak, underscoring the diminishing influence of plasmonic coupling as the dielectric layer thickens. Another point about this figure is related to the trend of the blueshift of the resonance wavelength for both modes. As it is shown in the figure, for both modes for thinner thickness from 10 to 30 nm, larger change in the resonance wavelength of around 130 nm is achieved, while by increasing the thickness from 30 to 60 nm is less than 30 nm. Therefore, it can be concluded that these modes are more sensitive to the gap layer thickness in the thinner dielectric gap layers.

These results indicate that the gap layer thickness plays a dual role in determining both the spectral position and the strength of the plasmonic modes. Based on these observations, the thickness of 40 nm was selected as the optimal gap layer thickness for achieving the strongest absorptance while maintaining a well-defined resonance peak.

1.3.2 Mode analysis

Figure 1.15 (a-d) illustrates the normalized electric field profiles for various modes across different gap layer thicknesses providing insights into their behavior under varying conditions. Nanohole diameter fixed on 440 nm, the angle of incident is zero and the thickness of the metal layer is 80 nm and metal nanohole array is 40 nm. For Mode I, a comparison of the field distribution across thicknesses from 10 nm to 40 nm shows the strongest field enhancement in the gap layer at 10 nm. Similarly, Mode II exhibits comparable trends, with field enhancement decreasing as the gap thickness increases. Additionally, for Mode II at 20 nm and 40 nm, some field localization occurs at the nanohole edges at the air interface. For thicknesses between 10 nm and 40 nm,

Mode II displays a distinct dipolar characteristic at longer wavelength resonances, while Mode I exhibits higher-order field distributions, with partial confinement at the air interface beyond the structure. These findings support the hypothesis that 1st and 2nd order diffraction couple with surface plasmon resonance (SPR) in the gap layer and partially interact with SPR excitation at the outer air-nanohole interface [41, 42].

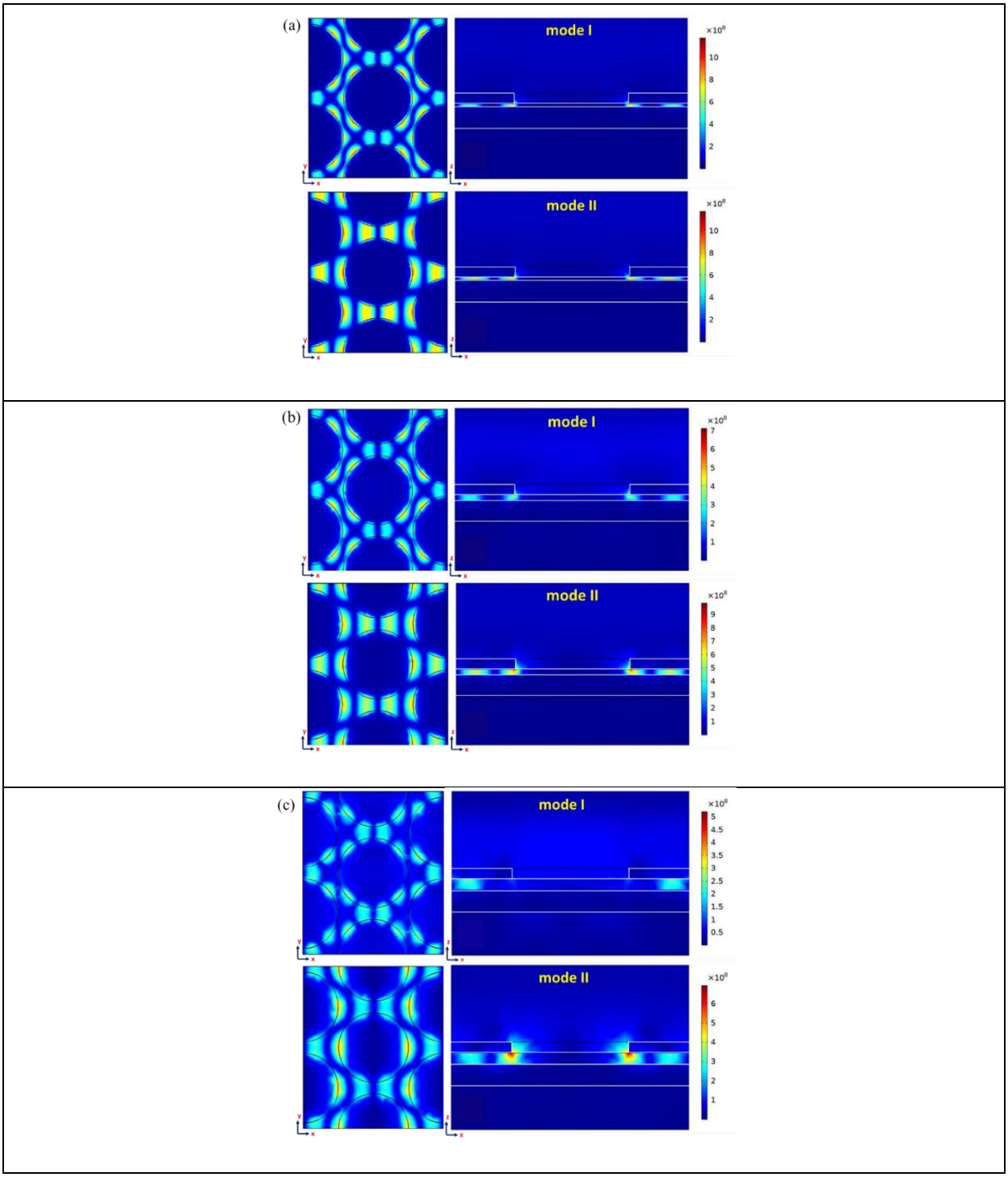

Figure 1.15 Normalized electric field distributions of the structure at various modes, shown in both xy and xz cross-sections, for gap layer thicknesses of (a) 10 nm, (b) 20 nm, and (c) 40 nm.

The study identifies two distinct resonance modes in the structure, influenced by geometric parameters, dielectric gap layer thickness, and angle of incidence. Mode II, a hybrid LSPR-GSP mode, exhibits strong absorptance, a significant redshift for thinner gap layers (10–30 nm), and maximum absorptance at normal incidence (0°). Its electric field is confined around nanohole edges and within the gap layer, with a dipole-like distribution and sensitivity to nanohole radius. Mode I, a higher-order GSP mode, shows weaker absorptance, no dependence on nanohole radius, and is visible only at small incidence angles (<10°), with a redshift and reduced absorptance as gap thickness increases. Electric field enhancement, measured as $|E|/|E_0|$, peaks for thinner gap layers but remains modest compared to other reported structures. These modes, showcasing a balance of localized and gap plasmonic effects, underscore the potential for tuning optical properties through precise structural adjustments, enabling applications in sensing, filtering, and energy harvesting.

1.3.3 Sensing properties

Figure 1.16 and Table 1.2 present the absorptance spectrum and sensitivity of the proposed structure with a 40 nm gap layer thickness for various analyte refractive indices. Given that the strongest absorptance occurs at a 40 nm thickness, this configuration was chosen to evaluate the structure's sensing capability. Figure 1.16 illustrates the absorptance spectrum of the structure when the analyte material, with a refractive index ranging from 1.33 to 1.53, replaces the air above the structure. As shown, resonance wavelength shifts are observed across three modes as the analyte refractive index changes. The measured sensitivities for these modes are summarized in Table 1.2.

Based on the measured sensitivities, Mode III exhibits a significant resonance wavelength shift with changes in the refractive index. Positioned in the visible range, this mode demonstrates high sensitivity, making it particularly suitable for sensing applications. Its strong sensitivity and visible-range positioning are ideal for detecting small refractive index changes. The reason this mode was not considered earlier is that it forms in the upper corners of the nanoholes, outside the gap layer, whereas the focus of this study is on the modes created within the dielectric gap layer. Mode I, in contrast, shows a moderate resonance wavelength shift and sensitivity (200 nm/RIU). Mode II positioned in the near-infrared range, displays the smallest resonance wavelength shift and the lowest sensitivity (150 nm/RIU), indicating limited utility for precise sensing applications. The strong field localization associated with Mode III directly correlates with its high sensitivity. This combination of sensitivity and visible-range resonance wavelength makes Mode I particularly advantageous for biochemical sensing applications, where detecting small refractive index variations is critical.

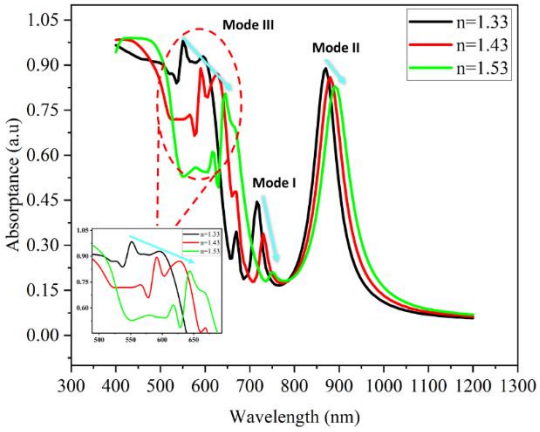

Figure 1.16 absorptance spectrum of the structure with 40 nm gap layer thickness with the different analyte refractive indexes

Table 1-2 sensitivity of the structure at different modes

	Mode I	Mode II	Mode III
S (nm/RIU)	200	150	400

1.4 3D structure with triangular gold nanodisks over a gold film

Plasmonic nanoantennas are gaining increasing attention for their ability to confine electromagnetic waves to sub-wavelength regions with significant field enhancement. This capability enables a wide range of advanced applications, including surface-enhanced Raman spectroscopy (SERS), single-molecule detection, photodetection, optical trapping, magnetic recording, and nanoscale light sources. The degree of field enhancement is crucial for the effectiveness of these applications. Among various nanoantenna designs, those composed of adjacent metallic nanoparticles with nanoscale gaps, such as bowtie nanoantennas, exhibit particularly strong field confinement and enhancement in the gap regions due to in-plane near-field coupling across the gaps[43]. Structural optimization techniques, including adjustment of gap size, antenna size, shape, and the formation of arrays, have been employed to further enhance field concentration and tailor the spectral response through in-plane near-field or far-field coupling mechanisms.

Plasmonic triangular nanodisks, with their sharp edges and corners, enable strong electromagnetic field confinement and enhanced local electric field intensity, making them promising for nanophotonic technologies. Their tunable geometric parameters, such as side length and apex angle, allow precise control over resonance wavelengths and spectral responses, enabling tailored designs for applications in sensing, imaging, and light manipulation. These structures also support versatile material integration, broadening their use in biosensing, catalysis, and optoelectronics. However, challenges like fabrication complexity, modeling limitations, and material uniformity must be addressed to unlock their full potential. Fabrication methods such as scanning, optical, and soft lithography offer precise nanostructure control but are costly, while colloidal lithography provides a cost-effective alternative for large-area metallic nanostructures. This study designed, simulated, and evaluated the optical behavior of metallic triangular nanodisks, demonstrating their suitability for fabrication via colloidal lithography.

In order to design and simulate the properties of the proposed structure all the setting and geometrical properties of the structure except the radius of the nanoholes, are similar to the previous part for nanohole array. In order to achieve triangular nanodisks the nanohole diameter is set to 500 nm. The designed structure is shown in figure 1.17.

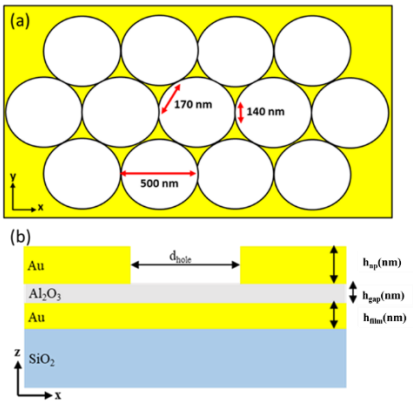

Figure 1.17 2D schematic of the structure from different view of (a) xy plain and (b) xz plain

1.4.1 Structure optimization

Figure 1.18 illustrates the absorptance spectrum of the plasmonic triangular nanodisk array structure with a 10 nm dielectric gap layer thickness as a function of the angle of incidence. As depicted in the figure, the absorptance reaches its maximum within two distinct wavelength ranges across all angles. The first range occurs at wavelengths shorter than 500 nm, while the second range lies between 1200 nm and 1300 nm, with particularly notable peak at 1250 nm. This resonance mode is likely related to the fundamntal localized plasmonic mode created within the gap layer.

Furthermore, the figure reveals that the triangular nanodisk array demonstrates angle independence across a broad angular range, from 0 to 80 degrees. Additionally, with an increase in the angle of incidence, the weaker resonance modes become more pronounced, indicating a change in the resonance behavior of the structure.

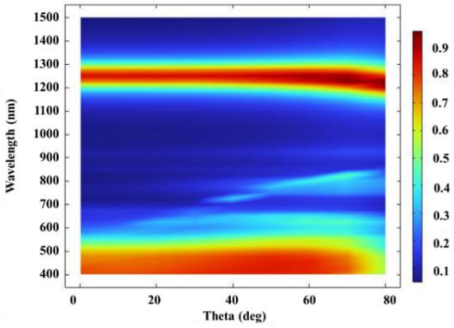

Figure 1.18 2D plot depicting the absorptance spectrum of the triangular structure as a function of the angle of incident light and 10 nm gap layer thickness

Figure 1.19 illustrates the absorptance spectrum of the plasmonic triangular nanodisk array structure as a function of the dielectric gap layer thickness. It is worth mentioning that, for this case, the angle of incidence of the light is set to zero degrees. As shown in this figure, at a 10 nm gap layer thickness, one sharp resonance mode is observed at wavelengths of 1250 nm. These observations are consistent with the results presented in Figure 1.19 for the zero-degree angle of incidence. By increasing the gap layer thickness from 10 nm to 20 nm, a significant shift in the resonance wavelength toward shorter wavelengths is observed. At this thickness, the resonance occurs at 1100 nm, and the absorptance is noticeably enhanced. When the thickness is further increased from 20 nm to 30 nm, another shift in the resonance wavelength is observed, although with a reduced slope compared to the earlier

transition. This results in an approximately 50 nm shift to shorter wavelengths, while the absorptance continues to increase. From 30 nm to 40 nm, no further shift in the resonance wavelength is observed, but the absorptance reaches its maximum value. Beyond this point, as the gap layer thickness is increased from 50 nm to 60 nm, the resonance wavelength has a slight continious shift toward longer wavelength and other peaks with weaker absorptance in shorter wavelength appeared. Therefore, based on these findings, a gap layers thickness of 10 nm could be chosen as the optimized thickness for applications requiring stronger absorptance and in cases we need more than one strong mode specially in the visible range 60 nm thickness is ideal.

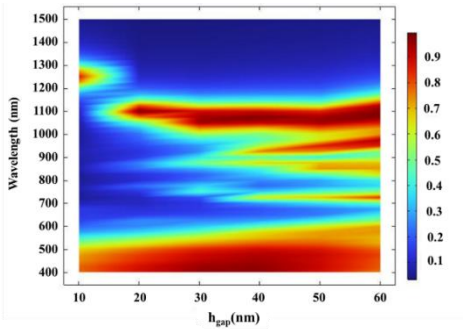

Figure 1.19 2D plot depicting the absorptance spectrum of the structure as a function of gap layer thickness (t_{gap})

1.4.2 Electric field enhancement

Electric field enhancement by optical structures is essential for amplifying light-matter interactions, enabling applications in sensing, spectroscopy, and nonlinear optics. Plasmonic structures are particularly significant in this regard, as they confine light to subwavelength scales and generate intense localized fields through surface plasmon resonances, greatly enhancing their utility in fields like biosensing and energy harvesting. In recent years, various plasmonic nanostructures have been proposed, and their capabilities for electric field enhancement have been evaluated. Yang Li et al. proposed an array of metal triangular nanodisks separated from a metal film by a dielectric layer. They compared this structure with circular and square nanodisk arrays and showed that the maximum electric field enhancement of 220 is achieved within the gap layer for the triangular nanodisk array [9]. Simón Roa et al. reported a theoretical analysis of the electric near-field enhancement in gold and silver nanodisk-based photonic crystals using the Finite-Difference Time-Domain (FDTD) method. Their results show that the enhancement factor $|E/E_0|^2$ strongly depends on geometrical parameters, reaching values of up to 1200 in the visible light spectrum [22]. In another study by Mohsenifard Atefeh et al., the electric field enhancement of an MIM structure with a hybrid grating of bowtie nanotriangles and cylindrical nanodisks was analyzed and compared. Their findings revealed that the structure optimized for near-field radiation with linear polarization at 800 nm wavelength achieves amplification in the gap space between the nanotriangle tips, with values ranging from a minimum of 188 to a maximum of 320 times [23]. However, the fabrication challenges associated with such structures prompted the exploration of alternatives to achieve similar enhancements with easier fabrication methods.

To evaluate the electric field enhancement capabilities of this structure and compare it with proposed structure in section 4.3, the $|E|/|E_0|$ for each sample was measured using COMSOL Multiphysics, and the results are presented in Table 1.3. The data indicate that a triangular nanodisk array with a 10 nm gap layer thickness exhibits stronger electric field enhancement in the gap layer under the dipolar resonance mode. Increasing the gap layer thickness from 10 to 40 nm significantly reduces the electric field enhancement in the dielectric layer. Comparing the electric field enhancement of the triangular nanodisk with a 10 nm gap layer thickness to recent works highlights that the proposed structure offers two key advantages: strong electric field enhancement and near-perfect

absorptance at its fundamental resonance mode. Additionally, the ease of fabrication of the triangular nanodisks using colloidal lithography, as demonstrated in this work, is an important feature, with the experimental results presented in Chapter 2.

Table 1-3 Electric field enhancemnt comparison of the proposed structures

	Triangular nanodisk-10nm gap	**Triangular nanodisk-40 nm gap**	**Nanohole array-10 nm gap**	**Nanohole array-40 nm gap**
$\|E\|/\|E_0\|$	310	170	56	20

2 Experimental results

2.1 Fabrication and characterization of gold nanoparticles

Here, Gold Nanoparticles with a thickness of 2 nm were deposited on a SiO_2 substrate by (PECVD) technique prepared at ÚEF FEI STU. In order to analyze the effect of annealing on the size and separation distance of the nanoparticles SEM images of the samples are presented in Figure 2.1(a,b) before and after annealing for 10 minutes at 300°C. The nanoparticles have island shape and an obvious size difference, due to the annealing of the samples, can be observed.

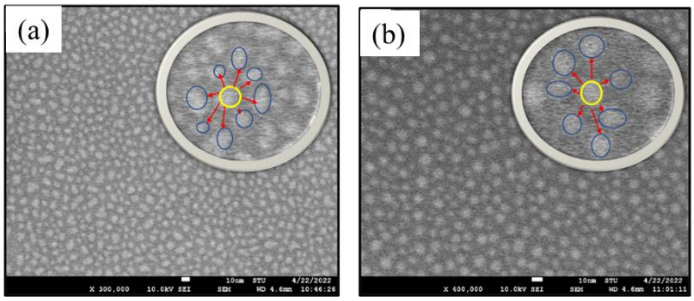

Figure 2.1 SEM image of the gold NPs (a) before annealing (b) after annealing at 300°C

The detailed analysis of the mentioned geometrical parameters is carried out from the SEM images using ImageJ software, as depicted in Table 2.1. The information about the diameter of the particles and their separation distance in this table is measured for 50 randomly chosen particles. Blue elliptical shapes show the nearest neighbors of one particle, and their distances are approximately calculated by measuring the length of the red vectors in Figure 2.1(a, b). By comparing the average diameter and average separation distance of the particles before and after annealing, it could be found that annealing the sample leads to the joining of the smaller particles to the larger particles and results in the large particle size and increasing the new particles separations.

Table 2-1 statical analysis of SEM image

	Before annealing	After annealing
Min particle diameter	5.48[nm]	6.45[nm]
Max particle diameter	12.84[nm]	10.31[nm]
Average particle diameter	8.41[nm]	8.11[nm]
Min particles separation	2.17[nm]	3.01[nm]
Max particle separation	9.32[nm]	13.84[nm]
Average particle separation	4.51[nm]	6.67[nm]

Moreover, the information in Table 5.1 indicates, after annealing the sample, the average particle diameter doesn't have a significant change, while these changes are remarkable for the maximum and minimum particle diameter. Therefore, we can conclude that, the size of the particles gets closer to the average size due to the annealing and all these evidences prove the influence of the annealing on having more homogenous gold NPs.

The graph in Figure 2.2 depicts the transmission of the gold NPs versus wavelength in the range of 300-800 nm, before and after annealing in different temperatures from 100°C to 300°C. The transmission spectra in Figure 2.2 have a minimum for all annealing temperatures due to the creation of the localized surface plasmon modes at their unique resonance wavelength. By increasing the temperature, the resonance wavelength shifts to the left, which shows the influence of the annealing temperature on the plasmonic phenomena. In fact, the reason of this influence is sensitivity of the LSPR to the size, shape and distribution of the gold NPs. However, by comparing the graph for annealing at 300°C for 10 minutes and 1 hour, it can be seen that there is a slight shift in the resonance wavelength. Therefore, we can conclude that the time duration of the heating does not have a significant impact on the wavelength resonance shift for the same temperatures. In Table 2.2, information about the resonance wavelength of the NPs in mentioned conditions is summarized.

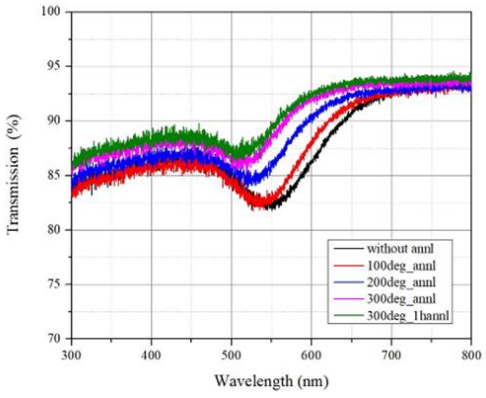

Figure 2.2 Transmission spectra of the Gold NPs before annealing and after that for different temperatures

Table 2-2 Resonance wavelength and minimum transmission of the NPs before and after annealing at different temperatures

	Resonance wavelength	**Minimum transmission**
Before annealing	545.20 [nm]	81.890 %
10 minutes at 100°	536.35 [nm]	82.703 %
10 minutes at 200°	519.36 [nm]	84.557 %
10 minutes at 300°	510.35 [nm]	86. 578 %
60 minutes at 300°	506.15 [nm]	87.006 %

2.2 Fabrication and characterization of metal triangular nanodisk and nanohole array over metal film

Here we tried to fabricate the proposed structures in section 1.3 and 1.4. to this end, after deposition of the gold film and dielectric layer by PECVD and ALD method respectively, the nanohole array were fabricated by colloidal lithography method. Figure 2.3 presents the final SEM images of the structure in two scenarios: one without etching the PS nanoparticles, resulting in triangular nanodisks, and the other with etching, leading to the formation of a metal nanohole array. Using this SEM images, we measured the approximate size of the nanoholes and the nano triangular nanodisks with Imagej software and used them in the simulations in sections 1.3 and 1.4.

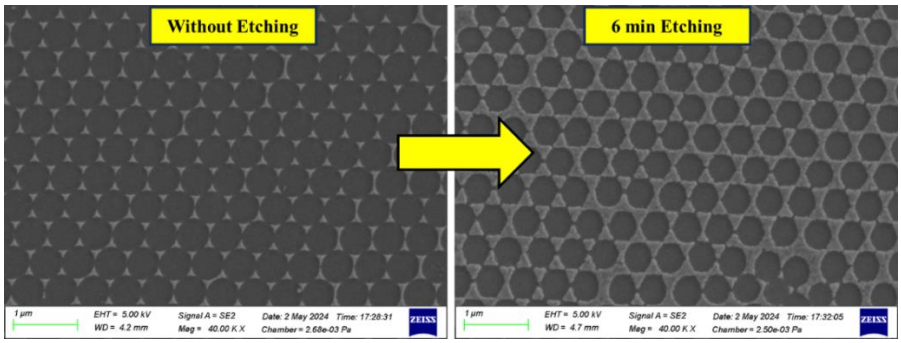

Figure 2.3 SEM picture of the prepared structure, triangular nanodisks (left) and hexagonal array of nanoholes (right)

2.2.1 Results and discussion

Figure 2.4(a) presents the reflectance spectrum of the structure without etching the polystyrene particles, consisting of triangular nanodisks. This Figure includes two graphs, each corresponding to different parts of the sample. For this sample, the gap layer thickness is 10 nm. A comparison between the simulation results presented in Figure 2.4(b) and experimental results reveals a similar dip in both graphs within the range of 500 nm to 1100 nm. However, as indicated in the simulation graph, one dip is observed at 1250 nm. The electric field distribution of the mode at 1250 nm confirms its association with dipolar resonance peaks. Due to the limitations of the measurement device, we were only able to measure the reflectance spectrum within this range. Therefore, our simulations predict the appearance of one peak in the infrared region, which can be verified in future studies.

However, similarity of the simulation and experimental results in the location of the resonance modes and even the percentage of absorptance at these two modes insure us for having the predicted resonance mode at 1250 nm. Based on the discussion in part 1.4.2, this resonance mode is the result of the coupling of the dipole created in the triangular nanodisk and its image in the metal film.

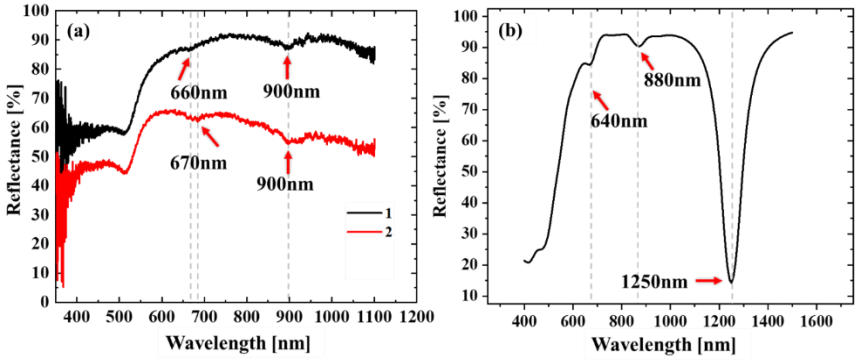

Figure 2.4 (a) Experimental and (b) simulated reflectance of the structure with triangular nanodisk and 10nm gap layer thickness

Increasing the gap layer thickness from 10 nm to 40 nm leads to a significant change in the reflectance spectrum of the structure with the same triangular nanodisks, as shown in Figure 2.5. In this Figure, measurements were performed five times on different areas of the sample. Based on the graph, all measurements show similar dips with slight variations in the resonance wavelength. A comparison between the experimental and simulation results represented in Figure 2.5(a, b) respectively, indicates similar dips at 555 nm in experimental results and 510 nm in simulation results. Similarly, another dip is observed at 665 nm in part (a) and at 685 nm in part (b). However, simulation results predict a dip at 820 nm which is absent in experimental results. Following this, a sharper dip appears at 1030 nm in the experimental results, while the same dip is observed at 1080 nm in the simulation results. Comparison of the reflectance spectrum of the structure with 10 nm and 40 nm gap layer thickness shows, that increasing of the gap layer thickness led to the decreasing of the reflectance percentage and increasing the modes with sharper dips as it was predicted and discussed in chapter 1. Based on the simulation and experimental results for these two thicknesses we can conclude that thicker gap layer thickness is ideal for sensing application that we need sharper dips in the visible range, while thinner gap layer thickness is suitable for strong electric field enhancement that was measured in chapter 1.

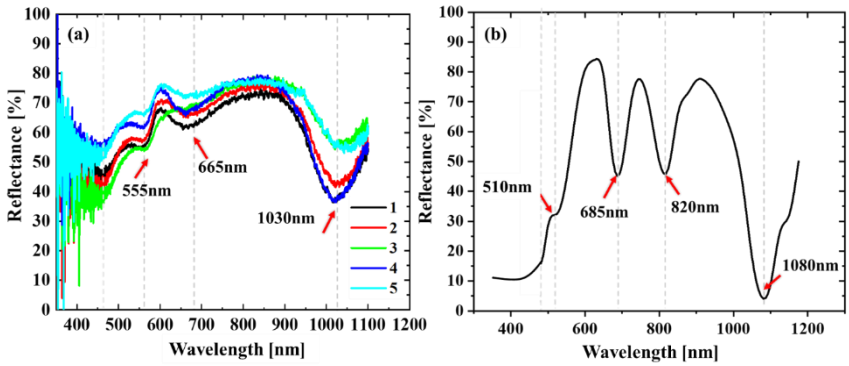

Figure 2.5 (a) Experimental and (b) simulated reflectance of the structure with triangular nanodisk and 40 nm gap layer thickness

In Figure 2.6, the polystyrene particles were etched for 6 minutes, resulting in a sample consisting of an array of gold nanoholes separated from a gold film by a 10 nm gap layer. A comparison between the experimental and simulation results reveals that, among the plasmonic modes predicted in the simulations, only the resonance mode at 500 nm is observed experimentally at 520 nm. This mode corresponds to the localized surface plasmon resonance (LSPR) generated at the upper edges of the nanoholes. The other two predicted modes at 850 nm and 1020 nm are associated with higher-order plasmonic modes. Additionally, the resonance mode predicted at 1275 nm, identified as a dipolar mode, lies outside the measurable range of the available equipment.

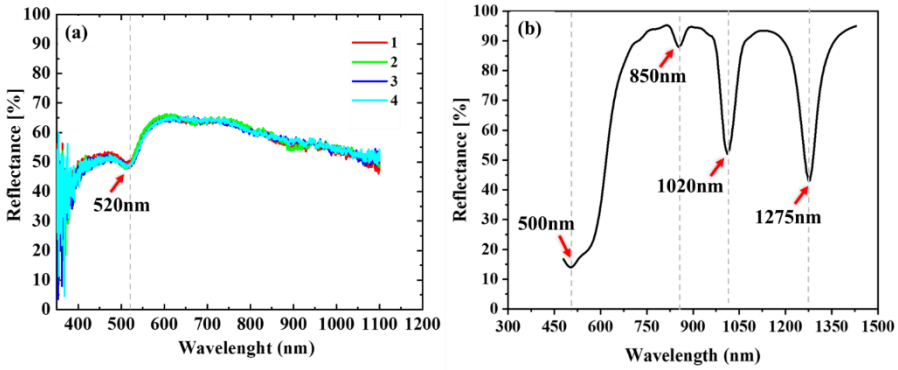

Figure 2.6 (a) Experimental and (b) simulated reflectance of the structure with nanohole array and 10nm gap layer thickness

In Figure 2.7, the sample is also an array of gold nanoholes but the gap layer thickness is increased to 40 nm. A comparison of the experimental and simulation results in parts (a) and (b) shows that the two observed peaks at 550 nm and 960 nm in the experimental data were predicted by the simulations, with a slight difference. However, the resonance mode predicted at 700 nm in the simulation results is not observed in the experimental data, likely because this mode is associated with higher-order plasmonic modes, as discussed in Chapter 1. Based on the discussion in Chapter 1, the peak observed at 960 nm in the experimental results corresponds to a hybrid LSPR-GSP mode. In contrast, the plasmonic mode observed at 550 nm is related to the localized surface plasmon resonance (LSPR) formed at the edges of the nanoholes, particularly at the upper edges. Comparision of the reflectance spectra in Figures 2.6 and 2.7 show that increasing the gap layer thickness lead to sharper dips and stronger absorptance which is ideal for sensing application and based on the discussion in chapter 1, this strucutre can not be very successful in field enhancment application.

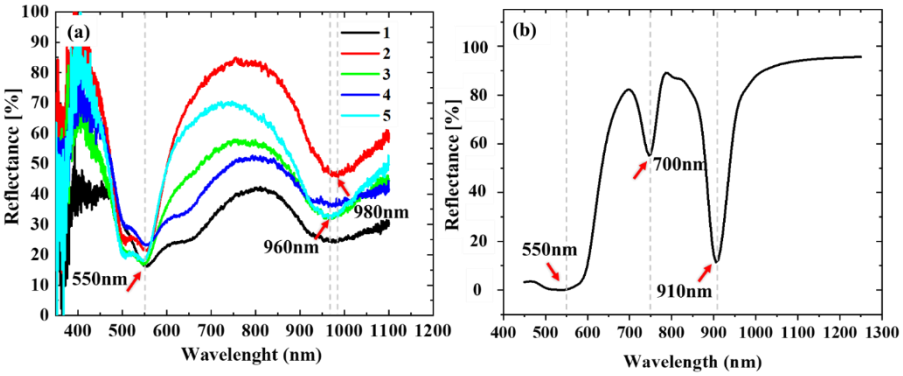

Figure 2.7 (a) Experimental and (b) simulated reflectance of the structure with nanohole array and 40nm gap layer thickness

Conclusion

Plasmonic nanostructures have emerged as a cornerstone of modern nanophotonics, offering unparalleled capabilities for manipulating light at the nanoscale. This thesis has explored their optical and sensing properties, emphasizing the critical interplay between design, fabrication, and application. This concluding section synthesizes the key insights derived from the extensive numerical simulations, experimental validations, and comprehensive analyses presented throughout the work.

1. Design Considerations

The design of plasmonic nanostructures revolves around optimizing their geometric and material parameters to achieve desired optical responses. The interplay between size, shape, and material composition dictates the resonance conditions of surface plasmon polaritons (SPPs) and localized surface plasmon resonances (LSPRs). For instance, structures such as gold nanodisks, nanostrips, and nanohole arrays exhibit distinct plasmonic behaviors that depend on their dimensional and spatial configurations. The simulations demonstrated that adjusting parameters such as particle height, gap thickness, and particles' separation distance significantly influences field enhancement and absorptance.

2. Fabrication Challenges and Techniques

Fabrication of plasmonic nanostructures translates theoretical designs into real devices, requiring precision and repeatability. The work utilized advanced techniques such as atomic layer deposition (ALD), colloidal lithography, and thin-film deposition to create structures with nanoscale accuracy. Each technique offers unique advantages: ALD enables uniform deposition of ultrathin dielectric layers, while colloidal lithography provides a scalable approach for creating periodic nanostructures. However, fabrication challenges persist, particularly regarding maintaining uniformity and minimizing defects. Variations in film thickness or nanoparticle shape can lead to deviations in the optical response, underscoring the need for precise control during fabrication. Integrating these methods with cutting-edge nanofabrication technologies, such as electron beam lithography or focused ion beam milling, could address these challenges, offering improved precision and expand design possibilities.

3. Optical Properties

Plasmonic nanostructures exhibit unique optical properties, characterized by enhanced electromagnetic fields and strong absorptance. These properties are exploited for applications such as SERS, sensing, and photonic devices. The resonance conditions of plasmonic structures were shown to be highly tunable, enabling selective manipulation of light in the visible and near-infrared ranges. For example, periodic nanodisk arrays demonstrated superior absorptance at fundamental resonance wavelengths, while nanostrip arrays offered sharper higher-order modes for wavelength-selective applications. Moreover, changing the gap layer thickness leads to the shift in resonance wavelength so, that fundamental resonance mode will occur at longer wavelength for thinner gap layer thickness than the structures with thicker gap layers. The electric field enhancement observed in the gap regions of these structures is particularly notable. Hotspots generated at these locations enable phenomena such as enhanced light-matter interaction and efficient energy conversion. This work has shown that tailoring the dimensions and configurations of nanostructures can achieve field enhancement factors exceeding 310, highlighting the potential for significant performance gains in optical applications.

4. Sensing Capabilities

One of the most promising applications of plasmonic nanostructures lies in sensing. The strong localized fields and resonance shifts induced by changes in the surrounding dielectric environment make these structures ideal for detecting minute variations in refractive index. Refractive index sensitivity, a critical parameter for evaluating sensing performance, was extensively analyzed.

The periodic nanostrip and nanodisk arrays showed comparable sensitivities at their fundamental resonance modes, with additional peaks observed for nanostrips, enabling multi-modal sensing. This thesis also demonstrated that optimizing geometric parameters such as gap thickness and nanoparticle size enhances sensing performance. Thinner gap layer thickness leads to the strongest electric field enhancement, while increasing the gap layer thickness enables the system to be considered in sensing applications. Additionally, the resonance wavelength shift provides a direct means of quantifying environmental changes, facilitating real-time sensing applications in areas like biosensing and chemical detection.

5. Applications and Future Directions

The findings presented in this thesis underscore the versatility of plasmonic nanostructures for diverse applications. Beyond sensing, these structures hold promise for solar energy harvesting, photothermal therapy, and advanced optical communication systems. Their ability to confine and manipulate light at the nanoscale offers opportunities for developing compact and efficient photonic devices. Future work could focus on integrating plasmonic structures with emerging technologies such as quantum dots or 2D materials, exploring hybrid systems that combine the advantages of different material platforms. Additionally, advancing fabrication techniques to enable large-scale production without compromising precision remains a critical goal. The development of machine learning-based optimization tools could further enhance design efficiency, enabling rapid prototyping of structures tailored for specific applications. In conclusion, this thesis has provided a comprehensive exploration of plasmonic nanostructures, emphasizing the critical interplay between design, fabrication, and application. By bridging theoretical insights with experimental validation, it contributes to advancing the field, paving the way for innovative solutions in nanophotonics and beyond.

Main results

1. **Optimization of MIM Structures with Elliptical Nanoparticles**; An optimized MIM structure with elliptical nanoparticles and a 5 nm ultrathin gap layer was developed and analyzed using a 2D simulation model. The study revealed that thinner gap layers (2-10 nm) result in smaller FWHM of the absorptance peak, enhancing sensing applications. Additionally, the particle separation distance was found to significantly influence electric field localization in the gap layer.
2. **Comparison of Circular Nanodisk and Nanostrip Arrays in MIM Structures**; Two MIM structures incorporating circular nanodisk arrays and metal nanostrip arrays were designed, optimized, and compared. Despite differences in nanoparticle shape, the 2D intersection of these structures resulted in similar optimized parameters, such as gap layer thickness, nanoparticle height, and angle of incident light. However, the distinct shapes of the nanoparticles led to variations in electric field enhancement and sensing capabilities. The structure with circular nanodisk array demonstrated greater potential for electric field enhancment application.
3. **Plasmonic Modes in MIM Structures with Nanohole Arrays**; The design, optimization, and analysis of plasmonic modes in an MIM structure with a plasmonic nanohole array were performed. 3D simulation results revealed that thicker gap layers enhance absorptance, making the structure more suitable for sensing applications.
4. **Plasmonic Modes in MIM Structures with Triangular Nanodisk Arrays**; An MIM structure with a plasmonic triangular nanodisk array was designed and optimized. 3D simulations showed that a gap layer thickness of 10 nm achieved the strongest electric field enhancement ($|E|/|E_0| = 310$) among all the proposed structures. Polarization dependency of the samples investigated and the results shows the Aabsorptance spectrum of the sturucture doesn't have a significent dependency on the polarization of incident light.

5. **Fabrication of Ultrathin Gold Nanoparticles**; Ultrathin gold nanoparticles were fabricated using the PECVD method, and the effects of annealing on their size, shape, and resonance wavelength were investigated. The experimental results revealed that annealing alters the particles' shape and size while achieving a more uniform distribution of particles.
6. **Fabrication and Characterization of MIM Structures with Nanohole Arrays**; MIM structures featuring plasmonic nanohole arrays were fabricated and characterized, focusing on variations in gap layer thickness. The results were consistent with simulation results.
7. **Fabrication and Characterization of MIM Structures with Triangular Nanodisk Arrays**; MIM structures incorporating plasmonic triangular nanodisk arrays were fabricated and characterized, with an emphasis on different gap layer thicknesses. The results were consistent with simulation results.

Resumé

Plazmonické nanoštruktúry sa ukázali ako základný kameň modernej nanofotoniky, ktorá ponúka bezkonkurenčné možnosti manipulácie so svetlom v nanoúrovni. Táto práca skúmala ich optické a snímacie vlastnosti, pričom zdôraznila kritickú súhru medzi dizajnom, výrobou a aplikáciou. Táto záverečná časť syntetizuje kľúčové poznatky odvodené z rozsiahlych numerických simulácií, experimentálnych validácií a komplexných analýz prezentovaných v práci.

1. Úvahy o dizajne

Návrh plazmonických nanoštruktúr sa točí okolo optimalizácie ich geometrických a materiálových parametrov, aby sa dosiahli požadované optické odozvy. Súhra medzi veľkosťou, tvarom a materiálovým zložením určuje rezonančné podmienky povrchových plazmónových polaritónov (SPP) a lokalizovaných povrchových plazmónových rezonancií (LSPR). Napríklad štruktúry, ako sú zlaté nanodisky, nanopásiky a polia nanodier, vykazujú odlišné plazmonické správanie, ktoré závisí od ich rozmerových a priestorových konfigurácií. Simulácie ukázali, že nastavenie parametrov, ako je výška častíc, hrúbka medzery a separačná vzdialenosť častíc, výrazne ovplyvňuje vylepšenie poľa a absorpciu.

2. Výrobné výzvy a techniky

Výroba plazmonických nanoštruktúr prevádza teoretické návrhy do skutočných zariadení, ktoré si vyžadujú presnosť a opakovateľnosť. Práca využívala pokročilé techniky, ako je depozícia atómovej vrstvy (ALD), koloidná litografia a depozícia tenkých vrstiev na vytvorenie štruktúr s presnosťou nanometrov. Každá technika ponúka jedinečné výhody: ALD umožňuje rovnomerné nanášanie ultratenkých dielektrických vrstiev, zatiaľ čo koloidná litografia poskytuje škálovateľný prístup na vytváranie periodických nanoštruktúr. Pretrvávajú však výrobné problémy, najmä pokiaľ ide o zachovanie jednotnosti a minimalizáciu defektov. Zmeny hrúbky filmu alebo tvaru nanočastíc môžu viesť k odchýlkam v optickej odozve, čo podčiarkuje potrebu presnej kontroly počas výroby. Integrácia týchto metód s najmodernejšími technológiami nanofabrikácie, ako je litografia s elektrónovým lúčom alebo frézovanie so zaostreným iónovým lúčom, by mohla vyriešiť tieto výzvy a ponúknuť vyššiu presnosť a rozšíriť možnosti dizajnu.

3. Optické vlastnosti

Plazmonické nanoštruktúry vykazujú jedinečné optické vlastnosti, ktoré sa vyznačujú zvýšenými elektromagnetickými poľami a silnou absorpciou. Tieto vlastnosti sa využívajú pre aplikácie ako SERS, snímanie a fotonické zariadenia. Ukázalo sa, že rezonančné podmienky plazmonických štruktúr sú vysoko laditeľné, čo umožňuje selektívnu manipuláciu so svetlom vo viditeľnom a blízkom infračervenom spektre žiarenia. Napríklad polia periodických nanodiskov preukázali vynikajúcu absorpciu pri základných rezonančných vlnových dĺžkach, zatiaľ čo polia nanopáskov ponúkali ostrejšie režimy vyššieho rádu pre aplikácie

selektívne pre vlnové dĺžky. Okrem toho zmena hrúbky vrstvy s medzerou vedie k posunu rezonančnej vlnovej dĺžky, takže základný rezonančný režim sa bude vyskytovať pri dlhšej vlnovej dĺžke pre tenšiu hrúbku vrstvy s dielektrickou medzerou ako štruktúry s hrubšími vrstvami s dielektrickou medzerou. Zvýšenie elektrického poľa pozorované v oblastiach dielektrickej medzivrstvy týchto štruktúr je obzvlášť pozoruhodné. Ohniskové body generované na týchto miestach umožňujú javy, ako je zvýšená interakcia svetla a hmoty a efektívna premena energie. Táto práca ukázala, že prispôsobením rozmerov a konfigurácií nanoštruktúr možno dosiahnuť faktory zosilnenia poľa presahujúce 310, čo zdôrazňuje potenciál pre výrazné zvýšenie výkonnosti v optických aplikáciách.

4. Senzorické schopnosti

Jedna z najsľubnejších aplikácií plazmonických nanoštruktúr spočíva v snímaní. Silné lokalizované polia a rezonančné posuny vyvolané zmenami v okolitom dielektrickom prostredí robia tieto štruktúry ideálnymi na detekciu nepatrných zmien indexu lomu. Citlivosť indexu lomu, kritický parameter na hodnotenie výkonnosti snímania, bola podrobne analyzovaná. Periodické polia nanopásikov a nanodiskov vykazovali porovnateľné citlivosti vo svojich základných rezonančných režimoch s ďalšími vrcholmi pozorovanými pre nanopásky, čo umožňuje multimodálne snímanie. Táto práca tiež ukázala, že optimalizácia geometrických parametrov, ako je hrúbka dielektrickej medzery a veľkosť nanočastíc, zvyšuje výkonnosť snímania. Tenšia hrúbka vrstvy dielektrickej medzery vedie k najsilnejšiemu zosilneniu elektrického poľa, zatiaľ čo zväčšenie hrúbky vrstvy dielektrickej medzery umožňuje, aby bol systém využívaný v aplikáciách snímania. Posun rezonančnej vlnovej dĺžky navyše poskytuje priamy spôsob na kvantifikáciu environmentálnych zmien, čo uľahčuje senzorické aplikácie v reálnom čase v oblastiach, ako je biosnímanie a chemická detekcia.

5. Aplikácie a budúce smerovanie

Zistenia prezentované v tejto práci podčiarkujú všestrannosť plazmonických nanoštruktúr pre rôzne aplikácie. Okrem snímania sú tieto štruktúry sľubné pre zber slnečnej energie, fototermálnu terapiu a pokročilé optické komunikačné systémy. Ich schopnosť obmedziť a manipulovať so svetlom v nanoúrovni ponúka príležitosti na vývoj kompaktných a efektívnych fotonických zariadení. Budúca práca by sa mohla zamerať na integráciu plazmonických štruktúr s novými technológiami, ako sú kvantové bodky alebo 2D materiály, skúmanie hybridných systémov, ktoré kombinujú výhody rôznych materiálových platforiem. Okrem toho, kritickým cieľom zostáva pokrok v technológiách výroby, aby bola umožnená výroba vo veľkom meradle bez kompromisov v presnosti. Vývoj optimalizačných nástrojov založených na strojovom učení by mohol ďalej zvýšiť efektivitu dizajnu, čo umožní rýchle prototypovanie štruktúr prispôsobených špecifickým aplikáciám. Na záver, táto práca poskytla komplexný prieskum plazmonických nanoštruktúr s dôrazom na kritickú súhru medzi dizajnom, výrobou a aplikáciou. Premostením teoretických poznatkov s experimentálnym overovaním prispieva k napredovaniu v tejto oblasti a dláždi cestu pre inovatívne riešenia v nanofotonike aj mimo nej.

Hlavné výsledky

1. Optimalizácia štruktúr MIM s eliptickými nanočasticami; Bola vyvinutá a analyzovaná optimalizovaná štruktúra MIM s eliptickými nanočasticami a 5 nm ultratenkou medzivrstvou pomocou 2D simulačného modelu. Štúdia odhalila, že tenšie vrstvy medzier (2-10 nm) vedú k menšiej pološírke maxima absorpcie, čo zlepšuje aplikácie snímania. Okrem toho sa zistilo, že vzdialenosť častíc významne ovplyvňuje lokalizáciu elektrického poľa v medzivrstve.

2. Porovnanie kruhových nanodiskov a nanopáskových polí v štruktúrach MIM; Boli navrhnuté, optimalizované a porovnané dve štruktúry MIM obsahujúce kruhové polia nanodiskov a polia kovových nanopásikov. Napriek rozdielom v tvare nanočastíc,

2D rezy týchto štruktúr viedli k podobným optimalizovaným parametrom, ako je hrúbka vrstvy medzery, výška nanočastíc a uhol dopadajúceho svetla. Odlišné tvary nanočastíc však viedli k zmenám v zvýšení elektrického poľa a senzorických schopností. Štruktúra s kruhovým poľom nanodiskov preukázala väčší potenciál pre aplikáciu zosilnenia elektrického poľa.

3. Plazmonické režimy v štruktúrach MIM s poľami nanodier; Uskutočnil sa návrh, optimalizácia a analýza plazmonických režimov v štruktúre MIM s poľom plazmonických nanodier. Výsledky 3D simulácie ukázali, že hrubšie medzivrstvy zvyšujú absorpciu, vďaka čomu je štruktúra vhodnejšia na senzorické aplikácie.

4. Plazmonické režimy v štruktúrach MIM s trojuholníkovými poliami nanodiskov; Bola navrhnutá a optimalizovaná štruktúra MIM s plazmonickým trojuholníkovým nanodiskovým poľom. 3D simulácie ukázali, že hrúbka vrstvy medzery 10 nm dosiahla najväčšie zosilnenie elektrického poľa ($|E|/|E_0| = 310$) spomedzi všetkých navrhovaných štruktúr. Polarizačná závislosť skúmaných vzoriek a výsledky ukazujú, že absorpčné spektrum štruktúry nemá významnú závislosť od polarizácie dopadajúceho svetla.

5. Výroba ultratenkých zlatých nanočastíc; Ultratenké zlaté nanočastice boli vyrobené metódou PECVD a skúmali sa účinky žíhania na ich veľkosť, tvar a rezonančnú vlnovú dĺžku. Experimentálne výsledky ukázali, že žíhanie mení tvar a veľkosť častíc, pričom sa dosahuje rovnomernejšia distribúcia častíc.

6. Výroba a charakterizácia štruktúr MIM s nanodierovými poľami; Boli vyrobené a charakterizované MIM štruktúry obsahujúce plazmmonické nanodierové polia so zameraním na variácie hrúbky medzivrstvy. Výsledky boli v súlade s výsledkami simulácie.

7. Výroba a charakterizácia štruktúr MIM s trojuholníkovými poliami nanodiskov; Boli vyrobené a charakterizované MIM štruktúry obsahujúce plazmonové trojuholníkové polia nanodiskov s dôrazom na rôzne hrúbky medzivrstvy. Výsledky boli v súlade s výsledkami simulácie.

References

1. Dormeny, A.A., P.A. Sohi, and M. Kahrizi, Design and simulation of a refractive index sensor based on SPR and LSPR using gold nanostructures. Results in Physics, 2020. **16**: p. 102869.
2. Li, Y., et al., Duplicating plasmonic hotspots by matched nanoantenna pairs for remote nanogap enhanced spectroscopy. Nano Letters, 2020. **20**(5): p. 3499-3505.
3. Zhu, Z., et al., Fano resonance boosted cascaded optical field enhancement in a plasmonic nanoparticle-in-cavity nanoantenna array and its SERS application. Light: Science & Applications, 2015. **4**(6): p. e296-e296.
4. Gurbatov, S., et al., Mapping the refractive index with single plasmonic nanoantenna. Scientific Reports, 2018. **8**(1): p. 3861.
5. Maier, S.A., Plasmonics: Fundamentals and Applications. 2007: Springer US.
6. Xu, Y., et al., Optical refractive index sensors with plasmonic and photonic structures: promising and inconvenient truth. Advanced Optical Materials, 2019. **7**(9): p. 1801433.
7. Mayer, K.M. and J.H. Hafner, Localized surface plasmon resonance sensors. Chemical reviews, 2011. **111**(6): p. 3828-3857.
8. Baumberg, J.J., et al., Extreme nanophotonics from ultrathin metallic gaps. Nature materials, 2019. **18**(7): p. 668-678.
9. Li, Y., et al., Achieving strong field enhancement and light absorption simultaneously with plasmonic nanoantennas exploiting film-coupled triangular nanodisks. The Journal of Physical Chemistry C, 2017. **121**(30): p. 16481-16490.
10. Wang, X., et al., Sensitive surface-enhanced Raman scattering detection using on-demand postassembled particle-on-film structure. ACS applied materials & interfaces, 2017. **9**(36): p. 31102-31110.
11. Sugimoto, H., S. Yashima, and M. Fujii, Hybridized plasmonic gap mode of gold nanorod on mirror nanoantenna for spectrally tailored fluorescence enhancement. Acs Photonics, 2018. **5**(8): p. 3421-3427.
12. Wang, B.-T. and Q. Wang, Sensitivity-enhanced optical fiber biosensor based on coupling effect between SPR and LSPR. IEEE Sensors Journal, 2018. **18**(20): p. 8303-8310.
13. Mock, J.J., et al., Probing dynamically tunable localized surface plasmon resonances of film-coupled nanoparticles by evanescent wave excitation. Nano Letters, 2012. **12**(4): p. 1757-1764.
14. Du, C., et al., Surface-enhanced Raman scattering from individual Au nanoparticles on Au films. Plasmonics, 2012. **7**(3): p. 475-478.
15. Mubeen, S., et al., Plasmonic properties of gold nanoparticles separated from a gold mirror by an ultrathin oxide. Nano letters, 2012. **12**(4): p. 2088-2094.
16. Nordlander, P. and E. Prodan, Plasmon hybridization in nanoparticles near metallic surfaces. Nano Letters, 2004. **4**(11): p. 2209-2213.
17. Srivastava, S.K., et al., Optimal interparticle gap for ultrahigh field enhancement by LSP excitation via ESPs and confirmation using SERS. The Journal of Physical Chemistry C, 2016. **120**(50): p. 28735-28742.
18. Aydin, K., et al., Broadband polarization-independent resonant light absorption using ultrathin plasmonic super absorbers. Nature communications, 2011. **2**(1): p. 517.
19. Lee, B.J., L. Wang, and Z. Zhang, Coherent thermal emission by excitation of magnetic polaritons between periodic strips and a metallic film. Optics Express, 2008. **16**(15): p. 11328-11336.
20. Chu, Y., M.G. Banaee, and K.B. Crozier, Double-resonance plasmon substrates for surface-enhanced Raman scattering with enhancement at excitation and stokes frequencies. ACS nano, 2010. **4**(5): p. 2804-2810.
21. Seok, T.J., et al., Radiation engineering of optical antennas for maximum field enhancement. Nano letters, 2011. **11**(7): p. 2606-2610.
22. Roa, S., G.E. Akinoglu, and M.L. Pedano, Electric field enhancement in Au and Ag nanodisks-based photonic crystals: Relevant design insights for efficient SERS substrates. Surfaces and Interfaces, 2023. **39**: p. 102948.
23. Atefeh, M. and M. Masoud, Increasing the electric field amplification in the metal-insulator-metal structure with a grating hybrid of bowtie nanotriangle and cylindrical nanodisc. Optik, 2024. **318**: p. 172083.
24. Kasap, S.O., Optoelectronics and photonics. 2013: Pearson Education UK.

25. Nicolas, R., et al., Plasmonic mode interferences and Fano resonances in Metal-Insulator-Metal nanostructured interface. Scientific reports, 2015. **5**(1): p. 14419.

26. Liu, D., et al., Terahertz composite plasmonic slabs based on double-layer metallic gratings. Optics Express, 2020. **28**(12): p. 18212-18223.

27. Chen, L.-S., et al., Design and Analysis of a Ag Rhombus Nanoparticle Film-Coupled Plasmonic Nanostructure. ACS omega, 2019. **4**(12): p. 14759-14764.

28. Gu, P., et al., Excitation and tuning of Fano-like cavity plasmon resonances in dielectric–metal core–shell resonators. Nanoscale, 2016. **8**(19): p. 10358-10363.

29. Lassiter, J.B., et al., Third-harmonic generation enhancement by film-coupled plasmonic stripe resonators. Acs Photonics, 2014. **1**(11): p. 1212-1217.

30. Huang, S., et al., Ultrasmall mode volumes in plasmonic cavities of nanoparticle-on-mirror structures. Small, 2016. **12**(37): p. 5190-5199.

31. West, P.R., et al., Searching for better plasmonic materials. Laser & photonics reviews, 2010. **4**(6): p. 795-808.

32. Singh, A.K., et al., Al2O3 as a suitable substrate and a dielectric layer for n-layer MoS2. Applied Physics Letters, 2015. **107**(5).

33. Zhu, W., et al., Quantum mechanical effects in plasmonic structures with subnanometre gaps. Nature communications, 2016. **7**(1): p. 1-14.

34. Jiang, N., X. Zhuo, and J. Wang, Active plasmonics: principles, structures, and applications. Chemical reviews, 2017. **118**(6): p. 3054-3099.

35. Li, J.F., et al., Shell-isolated nanoparticle-enhanced Raman spectroscopy. nature, 2010. **464**(7287): p. 392-395.

36. Chu, C.H., et al., Enhanced optical sensing with metal-insulator-metal nanohole arrays integrated with silver nanoparticles. Results in Physics, 2023. **55**: p. 107203.

37. Luo, X., et al., Sensitivity-improved SERS detection of methyltransferase assisted by plasmonically engineered nanoholes array and hybridization chain reaction. ACS sensors, 2020. **5**(11): p. 3639-3648.

38. Luo, X., et al., Boosting Long-range surface-enhanced Raman scattering on plasmonic nanohole arrays for ultrasensitive detection of MiRNA. ACS Applied Materials & Interfaces, 2021. **13**(15): p. 18301-18313.

39. Wong, Y.L., et al., Enhancing plasmonic hot-carrier generation by strong coupling of multiple resonant modes. Nanoscale, 2021. **13**(5): p. 2792-2800.

40. Tasnim, N. and A.S. Mohsin, Nanohole array integrated metal insulator metal (MIM) based structure employing dual mode SPR sensor for detection of Hemoglobin (Hb) in blood. Heliyon, 2024: p. e33445.

41. Stelling, C., et al., Surface plasmon modes of nanomesh-on-mirror nanocavities prepared by nanosphere lithography. Nanoscale, 2018. **10**(37): p. 17983-17989.

42. Jia, H., et al., Plasmonic nanohole arrays with enhanced visible light photoelectrocatalytic activity. Acs Photonics, 2022. **9**(2): p. 652-663.

43. Wang, B., et al., Design of aluminum bowtie nanoantenna array with geometrical control to tune LSPR from UV to near-IR for optical sensing. Plasmonics, 2020. **15**: p. 609-621.

Author's publication

ADC Scientific papers in foreign journals with impact factor

The number of records: 7

ADC01 **EBRAHIMZADEH ESFAHANI, Niloofar** - KOVÁČ, Jaroslav jr. - KOVÁČOVÁ, Soňa - FEILER, Martin. Plasmonic properties of the metal nanoparticles (NPs) on a metal mirror separated by an ultrathin oxide layer. **Photonics** 2023, 10(1), 78; doi: https://doi.org/10.3390/photonics1001007

ADC02 VAVRINSKY, Erik - **EBRAHIMZADEH ESFAHANI, Niloofar** - HAUSNER Michal - KUZMA Anton - REZO, Vratislav - DONOVAL Martin and KOSNACOVA Helena. The Current State of Optical Sensors in Medical Wearables. **Biosensors,** 2022, 12, 217. doi: 10.3390/bios12040217

ADC03 **EBRAHIMZADEH ESFAHANI, Niloofar** - KOVÁČ, Jaroslav jr - MARUCCIO, Giuseppe - RIZZATO, Silvia - KOVÁČOVÁ, Soňa .Comparative Analysis of Two Different MIM Configurations of a Plasmonic Nanoantenna. **Plasmonics** (2024); doi: https://doi.org/10.1007/s11468-024-02528-6

Collaboration with other groups:

ADC04 SADEGHI, Behzad - CAVALIERE, Pasquale - BAYAT, Mutlucan - **EBRAHIMZADEH ESFAHANI, Niloofar** - LASKA, Aleksandra - KOSZELOW, Damian. Experimental study and numerical simulation on porosity dependent direct reducibility of high-grade iron oxide pellets in hydrogen. International Journal of Hydrogen Energy (2024), Volume 69, 5 June 2024, Pages 586-607; doi: https://doi.org/10.1016/j.ijhydene.2024.05.050.

ADC05 ZIAEI Hosein - **EBRAHIMZADEH ESFAHANI, Niloofar** - MARFAVI, Zeinab - SADEGHI, Behzad - CAVALIERE, Pasquale .Crystal structure evolution in mehcanical alloying and spark plasma sintering of AlxCoCrCuFeNi HEAs. Powder Metallurgy ,64, 2021 - Issue 1. doi: 10.1080/00325899.2020.1857954.

ADC06 SADEGHI, Behzad - AZIMI ROEEN, Ghasem - NOSKO, Martin - SHAMANIAN, Morteza - TREMBOSOVA, Veronika - NAGY, Štefan - **EBRAHIMZADEH ESFAHANI, Niloofar**. Hot rolling of MWCNTs reinforced Al-matrix composites produced via spark plasma sintering. **Advanced Composites and Hybrid Materials,** 2, pages 549–570 (2019), doi: 10.1007/s42114-019-00095-7.

ADC07 ZIAEI, Hosein - **EBRAHIMZADEH ESFAHANI, Niloofar** - MARFAVI, Zeinab - SADEGHI, Behzad - CAVALIERE - Pasquale. Phase evolution in mechanical alloying and spark plasma sintering of AlxCoCrCuFeNi HEAs. **Powder metallurgy**, 36, 5, 2020.

AFC Published papers at foreign scientific conferences

The number of records: 1

AFC01 **EBRAHIMZADEH ESFAHANI, Niloofar** - KOVÁČOVÁ, Soňa - FEILER, Martin - KOVÁČ, Jaroslav jr. Optical properties of gold nanoparticles for SERS substrates prepared by PVD technique. 2nd Global Summit and Expo on Laser, Optics and Photonics (GSELOP2022), August 2022, Edinburgh, Scotland.

AFD Published papers at domestic scientific conferences

The number of records: 3

AFC01 **EBRAHIMZADEH ESFAHANI, Niloofar** - FEILER, Martin - KOVÁČ, Jaroslav jr - KOVÁČOVÁ, Soňa. Strong field enhancement and Sensing capability of the film coupled nanoparticle plasmonic-based structure. 10th international conference on Advances in Electronic and Photonic Technologies, June 2022, High Tatras, Slovakia. (3rd place award in student oral presentation competition).

AFC02 **EBRAHIMZADEH ESFAHANI, Niloofar** - KOVÁČOVÁ, Soňa - KOVÁČ, Jaroslav jr – PODLUCKY Lubos, .Annealing effect on the size and separation distance of the gold nanoparticles deposited on a SiO_2 substrate.

Proceedings of ELITECH ’24th Conference of Doctoral Students June 1, 2022, FEI STU, Bratislava, Slovakia. (2nd place award in student oral presentation competition).

AFC03 **EBRAHIMZADEH ESFAHANI, Niloofar -** KOVÁČOVÁ, Soňa - KOVÁČ, Jaroslav jr. Optical response of a particle on mirror structure using various plasmonic materials. 11th international conference on Advances in Electronic and Photonic Technologies, June 2023, High Tatras, Slovakia.